




2019

## MODELING THE CONDENSED-PHASE BEHAVIOR OF $\pi$ - CONJUGATED POLYMERS

Walker Mask

University of Kentucky, walker.mask@outlook.com

Author ORCID Identifier:

 <https://orcid.org/0000-0002-0911-857X>

Digital Object Identifier: <https://doi.org/10.13023/etd.2020.033>

[Right click to open a feedback form in a new tab to let us know how this document benefits you.](#)

### Recommended Citation

Mask, Walker, "MODELING THE CONDENSED-PHASE BEHAVIOR OF  $\pi$ -CONJUGATED POLYMERS" (2019).  
*Theses and Dissertations--Chemistry*. 120.  
[https://uknowledge.uky.edu/chemistry\\_etds/120](https://uknowledge.uky.edu/chemistry_etds/120)

This Master's Thesis is brought to you for free and open access by the Chemistry at UKnowledge. It has been accepted for inclusion in Theses and Dissertations--Chemistry by an authorized administrator of UKnowledge. For more information, please contact [UKnowledge@lsv.uky.edu](mailto:UKnowledge@lsv.uky.edu).

## **STUDENT AGREEMENT:**

I represent that my thesis or dissertation and abstract are my original work. Proper attribution has been given to all outside sources. I understand that I am solely responsible for obtaining any needed copyright permissions. I have obtained needed written permission statement(s) from the owner(s) of each third-party copyrighted matter to be included in my work, allowing electronic distribution (if such use is not permitted by the fair use doctrine) which will be submitted to UKnowledge as Additional File.

I hereby grant to The University of Kentucky and its agents the irrevocable, non-exclusive, and royalty-free license to archive and make accessible my work in whole or in part in all forms of media, now or hereafter known. I agree that the document mentioned above may be made available immediately for worldwide access unless an embargo applies.

I retain all other ownership rights to the copyright of my work. I also retain the right to use in future works (such as articles or books) all or part of my work. I understand that I am free to register the copyright to my work.

## **REVIEW, APPROVAL AND ACCEPTANCE**

The document mentioned above has been reviewed and accepted by the student's advisor, on behalf of the advisory committee, and by the Director of Graduate Studies (DGS), on behalf of the program; we verify that this is the final, approved version of the student's thesis including all changes required by the advisory committee. The undersigned agree to abide by the statements above.

Walker Mask, Student

Dr. Chad Risko, Major Professor

Dr. Yinan Wei, Director of Graduate Studies

MODELING THE CONDENSED-PHASE BEHAVIOR  
OF  $\pi$ -CONJUGATED POLYMERS

---

THESIS

---

A thesis submitted in partial fulfillment of the  
requirements for the degree of Master of Science in the  
College of Arts and Sciences  
at the University of Kentucky

By

Walker Mask

Lexington, Kentucky

Director: Dr. Chad Risko, Professor of Chemistry

Lexington, Kentucky

2019

Copyright © Walker Mask 2019  
<https://orcid.org/0000-0002-0911-857X>

## ABSTRACT OF THESIS

### MODELING THE CONDENSED-PHASE BEHAVIOR OF $\pi$ -CONJUGATED POLYMERS

It is well established that the morphology and physical properties of an organic semiconducting (OSC) material regulate its electronic properties. However, structure-function relationships remain difficult to describe in polymer-based OSC, which are of particular interest due to their robust mechanical properties. If relationships among the molecular and bulk levels of structure can be found, they can aid in the design of improved materials. To explore and detail important structure-function relationships in polymer-based OSC, this work employs molecular dynamics (MD) simulations to study various  $\pi$ -conjugated polymers in different environments. Two independent investigations are discussed in this work. One investigation examines how the purposeful disruption of the  $\pi$ -conjugated backbone to increase the chain flexibility impacts the chain structure and packing in the condensed phase. This is done by adding a conjugation break spacer (CBS) unit of one to ten carbons in length into the monomer structure of diketopyrrolopyrrole-based polymers. It is found that trends in the folding and glass structure follow the increase and the parity (odd versus even) of the CBS length. The second investigation analyzes a variety of polymers and small molecule acceptor (SMA) blends to observe the effects of changing the shape of either component and the physical properties of the material, as well as the structure of the polymer chains. It is found that the conjugated core, the side chains, and the planarity or sphericity each influence the density and diffusion of the materials made.

KEYWORDS: Conjugated Polymers, Organic Semiconductors, Computational Chemistry, Molecular Dynamics, Polymer Morphology, Polymer Folding

Walker Mask

---

*(Name of Student)*

12/19/2019

---

Date

MODELING THE CONDENSED-PHASE BEHAVIOR  
OF  $\pi$ -CONJUGATED POLYMERS

By  
Walker Mask

Dr. Chad Risko  
\_\_\_\_\_  
Director of Thesis

Dr. Yinan Wei  
\_\_\_\_\_  
Director of Graduate Studies

12/19/2019  
\_\_\_\_\_  
Date

## ACKNOWLEDGMENTS

The following thesis, while an individual work, benefited from the insights and direction of several people. First, my Thesis Chair, Dr. Chad Risko, without the guidance and support of whom I could not have completed this work anywhere near on time. Thank you for giving me the chance to learn and to push myself. Next, I wish to thank the complete Thesis Committee: Dr. Christopher Richards, Dr. Jason DeRouchey, and Dr. Thomas Dziubla. I also want to recognize my fellow graduate students in the Risko Group, Shi Li, Qianxiang (Alex) Ai, Josiah Roberts, and Chamikara Karunasena, for the many insightful discussions, suggestions, guidance, and mid-afternoon distractions.

In addition to the scientific and emotional assistance above, I received equally important support from family and friends. My parents, brothers, and many friends from my undergraduate family at Simpson College all had to endure me talking about research problems that they understood very little to none about, and I thank them so dearly for being patient. I also could not have finished this task without the support of my friends here at the University of Kentucky, whose own research sometimes inspired me to use a new perspective for my own work. Lastly, I want to thank the faculty at Simpson College than directly influenced my path in the sciences: Professors Lindsay Ditzler, Derek Lyons, Heidi Berger, Aaron Santos, Murphy Waggoner, Katherine Vance, Jan Everhart, and Coryanne Harrigan. Without their mentoring I would not be at this school to write this thesis and not be as successful as I am.

## TABLE OF CONTENTS

ACKNOWLEDGMENTS .....	iii
LIST OF TABLES .....	v
LIST OF FIGURES .....	vi
CHAPTER 1: ORGANIC SEMICONDUCTORS .....	1
1.1 Key Electronic Properties in OSC .....	1
1.2 Bulk Properties and Device Structure.....	3
1.3 Folding and Structure of Conjugated Polymers.....	6
CHAPTER 2. COMPUTATIONAL METHODS: THEORY AND TECHNIQUES.....	8
2.1 Molecular Dynamics.....	8
2.1.1 Force Fields.....	9
2.1.2 Simulation Workflow.....	12
2.2 Density Functional Theory .....	14
CHAPTER 3. DISRUPTING THE BACKBONE $\pi$ -CONJUGATION IN DPP-BASED POLYMERS 15	
3.1 Introduction.....	15
3.2 Methods.....	16
3.3 Results and Discussion .....	18
3.3.1 Vacuum Simulations.....	18
3.3.2 Condensed-Phase Simulations.....	22
3.4 Conclusions.....	31
CHAPTER 4. BEHAVIOR OF POLYMER AND SMALL MOLECULE BLENDS ....	33
4.1 Introduction.....	33
4.2 Methods.....	35
4.3 Results and Discussion .....	37
4.4 Conclusions.....	41
CHAPTER 5. CONCLUSIONS AND FUTURE WORK.....	43
REFERENCES .....	45
VITA.....	49

## LIST OF TABLES

Table 1.1: Characteristic ranges of conductivity and the band gap for various materials ..	3
Table 3.1: Atom counts and weights for the DPP-4T and DPP-m polymer chains.....	16
Table 3.2: Compression and decompression steps for the condensed-phase systems .....	17
Table 3.3: Start and end values of the radius of gyration for the collapse trajectories.....	19
Table 3.4: Collapse rate in nm/ps of single polymer chains in vacuum .....	20
Table 3.5 Average densities for the single-component glass systems .....	24
Table 3.6: MSD-derived self-diffusion coefficients for the single-component bulk systems .....	26
Table 3.7: Radius of gyration for DPP-m in different condensed-phase systems .....	27
Table 3.8: Radius of gyration for DPP-4T in different condensed-phase systems .....	28
Table 4.1: Atom Counts and weights for polymer and SMA species.....	35
Table 4.2: Mass percent SMA for the systems not at equal mass ratio .....	36
Table 4.3: Compression and decompression steps for all systems investigated.....	37
Table 4.4: Computerd metrics for the sinlge-component polymer and SMA systems .....	38
Table 4.5: Calculated densities for the various polymer:SMA blends .....	39
Table 4.6: Calculated MSD-derived diffusion for the various polymer:SMA blends.....	41



## LIST OF FIGURES

Figure 1.1: Evolution of the molecular energy levels into bands from ethylene to trans-polyacetylene .....	2
Figure 1.2: Diagrams of generic representations of organic electronic devices .....	4
Figure 1.3: Internal structure of the OSC material in an OPV device .....	6
Figure 1.5: Common chain structures for $\pi$ -conjugated polymers .....	7
Figure 2.1: Algorithm for determining atomic movement in each step of MD .....	9
Figure 2.2: Representations of the internal coordinates for the bonded interaction terms in an interatomic potential.....	10
Figure 3.1: Structures of polymers DPP-4T and DPP-m.....	15
Figure 3.2: Radius of gyration (nm) versus time (ps) for the collapse of all DPP-based polymers in vacuum.....	18
Figure 3.3: Radius of gyrations versus time for all DPP-m collapse trajectories .....	20
Figure 3.4: Dihedral angle distribution for the sulfur-carbon-carbon-sulfur dihedral angle between the thiophene rings in DPP-4T .....	21
Figure 3.5: Sulfur-carbon-carbon-sulfur angle distributions for the DPP-m moieties .....	22
Figure 3.6: Density versus increasing CBS length .....	23
Figure 3.7: Determination of the glass transition temperature for the DPP-based polymers .....	25
Figure 3.8: Simulation snapshots for selected polymers .....	28
Figure 3.9: Inter-thiophene dihedral angle distributions for all simulated DPP-4T polymers .....	30
Figure 3.10: Simulation snapshots of the multi-component DPP-4T in DPP-m .....	30
Figure 3.11: Comparisons of the thiophene-thiophene angle for DPP-m moieties in all simulations .....	31
Figure 4.1 Structures of the BHJ component species investigated in this work.....	34

## CHAPTER 1: ORGANIC SEMICONDUCTORS

### 1.1 Key Electronic Properties in OSC

The development of new energy-harnessing, storing, and transporting materials can be supported by data from computational models. For organic semiconductors (OSC), understanding how changes to the molecular structure influence changes in electronic and physical properties of both single molecules, bulk materials, and blends of many materials can help guide future development. If computational models that are shown to be representative of experiment can be established, many prospective materials can be designed without requiring physical synthesis and fabrication, saving resources.

The ability of certain organic species to move charges relies on an extended system of  $\pi$ -orbitals, a pattern referred to as  $\pi$ -conjugation. The simplest  $\pi$ -conjugated molecule is ethylene,  $C_2H_4$ . Assuming a linear combination technique of molecular orbitals similar to that which can be done with the linear combination of atomic orbitals (LCAO), ethylene can be observed as the product of the bonding between the  $\pi$ -orbitals of two methyl radicals. The linear combination produces two new molecular orbitals from the two methyl radical  $\pi$  orbitals. The lower energy combination is the highest occupied molecular orbital (HOMO) and the higher energy combination is the lowest unoccupied molecular orbital (LUMO). The distance between these two energy levels is known as the fundamental gap. For ethylene, the optical gap  $E_{opt}$ , which is related to the fundamental gap, has been determined to be approximately 7 eV, or 160 kcal/mol. Similar to using a methyl radical to create ethylene, butadiene,  $C_4H_6$ , can be thought of as the bonding between two ethylene molecules via a single bond. The same is true for  $C_6H_8$ ,  $C_8H_{10}$ ,  $C_{10}H_{12}$ , and so on.

As more conjugated units are added onto a single molecule, the energy of  $E_{opt}$  decreases. The addition of more units also reduces the space between the all the various molecular orbitals below the HOMO and above the LUMO. These levels eventually become indistinguishable and the collective energy range covered by all the levels is known as a band. The  $\pi$  levels below the HOMO become the valence band, and the  $\pi$  levels above the LUMO become the conduction band. This evolution is shown in Figure 1.1. The energy at the top of the valence band, previously the HOMO, is the ionization potential (IP), and the energy at the bottom of the conduction band, previously the LUMO, is the electron affinity (EA). The distance between the two bands is the band gap,  $E_g$ . Theoretically, this suggests that an infinite conjugated chain should have an  $E_g$  of 0 eV. However the measured gap for the resulting polymer, trans-polyacetylene, is 1.5 eV.<sup>1</sup> This is a result of the bond length alternation (single and double bonds) resulting in different geometries for different energy levels in the molecule. This residual gap is what classifies trans-polyacetylene, and many  $\pi$ -conjugated polymers, as semiconducting materials.

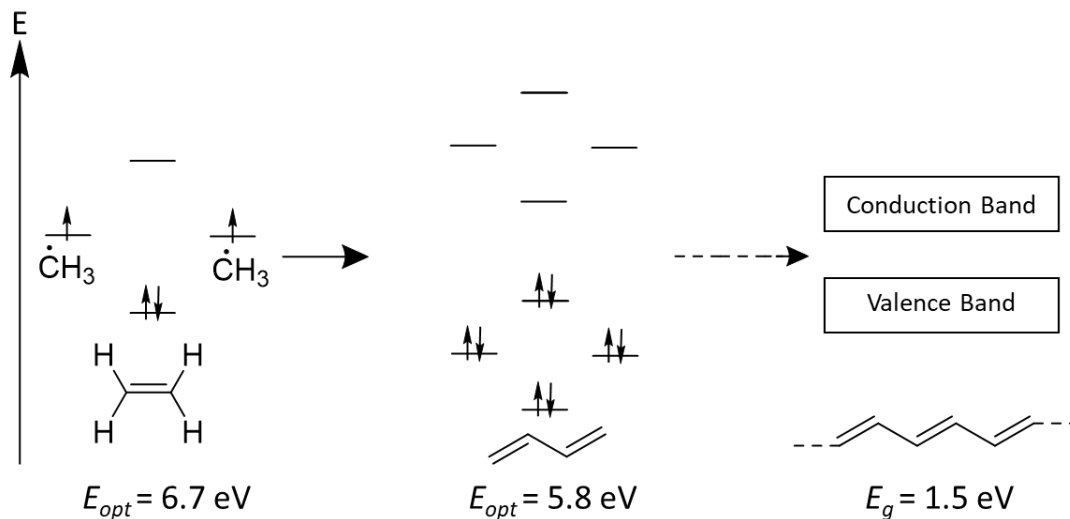


Figure 1.1: Evolution of the molecular energy levels into bands from ethylene to trans-polyacetylene.

A material's electrical properties determine its effectiveness as an OSC. Electrons crossing the band gap from the valence band up to the conduction band results in electrical current, and the ability for this to happen can be measured as conductance. Metals have an  $E_g$  of 0 eV, meaning that current in metals can be achieved through thermal excitations alone since the IP and EA are at the same value. The goal then is to push towards metallic conductivity while retaining the deformability and stability of polymeric materials.<sup>2</sup>

Conductivity can be thought of in a 'phenomenological' sense as the product of three properties, shown in equation (1). The charge carrier density,  $\eta$ , is the number charges in a material per unit volume, with the standard unit of inverse cubic centimeters. Charge carrier mobility,  $\mu$ , is a measure of how fast charges move through the material, and is derived from the average speed of diffusion of charge (cm/sec) as a function of an applied electric field (V/cm). Since charges are involved in the other factors but not accounted for in units, the third component is charge itself,  $q$ . Thinking of conductivity as the product of these properties has the consequence of relating mobility and charge density indirectly, such that a material with low density and high mobility can give the same conductivity as a material with high density and low mobility. For metals, the (Drude) model of electrons moving freely in an atomic lattice results in very high density with relatively low mobility, giving high conductance.<sup>3</sup> For semiconducting materials, having low or high mobility is directly related to improved device performance, given all other factors held constant.

$$\sigma \left( \frac{S}{cm} \right) = \eta \left( \frac{1}{cm^3} \right) * \mu \left( \frac{cm^2}{V \cdot sec} \right) * q(C), \quad S = \frac{1}{\Omega} = \frac{C}{V \cdot sec} \quad (1)$$

Conductance and the band gap are thus two metrics that materials can be classified by that also describe their electronic properties. The band gap considers the molecular-like electronic characteristics and the conductance considers the bulk material property. The values of these properties, listed in Table 1.1, determine whether the material is considered to be an insulator, semiconductor, or metal (highly conductive). It is significant to note that the table shows room-temperature ranges for conductivity. There are many species of both metals and semiconductors that shows superconductivity at very low temperatures (the conductivity of silver at 20°C is  $6.3 \times 10^9$  S/cm). For metals, increasing the temperature increases their mobility, thus decreasing conductivity, the opposite effect occurs for insulators and semiconductors. Many  $\pi$ -conjugated organic species fall into the insulator and low semi-conductor range, and can achieve higher conductivity upon doping or blending with other semiconducting materials. The trends suggest that to achieve a more conductive material, chemists can look to finding ways to close the band gap or increasing the mobility of semiconductors.

Table 1.1: Characteristic ranges of conductance and the band gap for various materials.

	Band Gap, $E_g$	Room-Temperature Conductivity, $\sigma_{RT}$
Insulators	$2 \text{ eV} \leq E_g$	$\sigma_{RT} \leq 10^{-10} \text{ S/cm}$
Semiconductors	$0 \text{ eV} < E_g \leq 2 \text{ eV}$	$10^{-10} \text{ S/cm} \leq \sigma_{RT} \leq 10^2 \text{ S/cm}$
Metals	$E_g \rightarrow 0 \text{ eV}$	$10^2 \text{ S/cm} \leq \sigma_{RT}$

## 1.2 Bulk Properties and Device Structure

A field-effect transistor (FET) is an electronic device that utilizes electric current to control the flow of charge. These types of devices utilize either electrons or holes to move charge (negative or positive, respectively) based on the type of voltage applied. All field-effect transistors are comprised from semi-conductive materials, a substrate, and three electrodes: source, drain, and gate. These components are arranged in different configurations with respect to the layering and processing of the materials. If the device is made with an organic semiconductor, it is known as an organic field effect transistor (OFET). OFETs can adopt the structure of the thin-film transistor, the structure of which is shown in Figure 1.2. The thin-film devices have the source and drain electrodes deposited directly onto the OSC material and a dielectric layer that separates the gate electrode from the OSC. The type of voltage applied to the gate ( $V_g$ ) and drain ( $V_D$ ) electrodes dictate the type of charge carrier injected into the material. If  $V_g$  is positive, then negative charges accumulate in the OSC, and the opposite occurs for a negative  $V_g$ . When  $V_D$  is then applied in the same parity (even versus odd), transport is achieved for the accumulated electrons or holes. The OSC can be designed to transfer either electrons or holes specifically, which are often referred to as p-channel and n-channel, respectively.

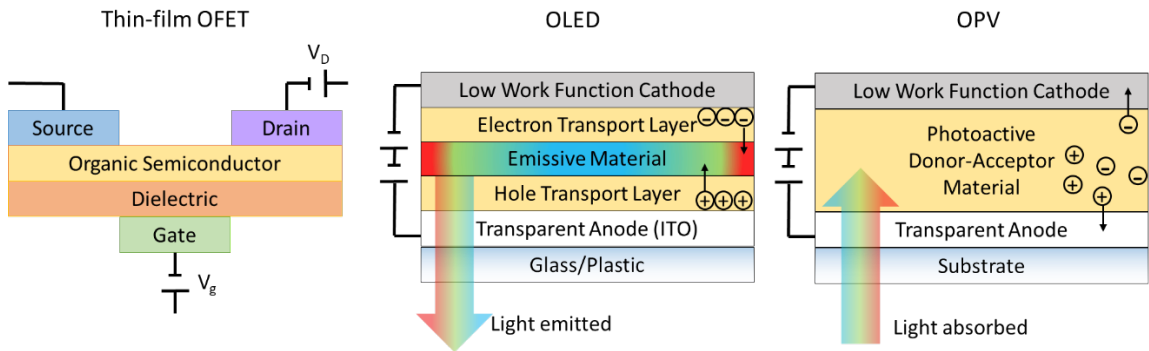


Figure 1.2: Diagrams of generic representations of organic electronic devices. LEFT: Top-contact-bottom-gate OFET structure; the parity of the voltage at the gate and drain electrodes determines the type of charge injected into the OSC material. MIDDLE: OLED structure, showing the movement of holes and electrons into the emissive layer to produce light. RIGHT: OPV structure, showing the absorption of light into a photoactive OSC material that will produce charges.

An additional application of OSC materials is the organic light emitting-diode (OLED). These devices require additional materials when compared to an OFET, and a common structure is shown in Figure 1.2. These devices operate by combining free electrons and holes on the same molecule to form an excited state species, which then relaxes and releases photons. The most common reported metric for OLEDs is the external quantum efficiency (EQE), which is the ratio of the number of photons that are released as light vs the number of electrons injected into the OSC material. Designing toward optimizing the EQE has led to trends in the development of new materials that incorporate using both phosphorescence and fluorescence, or different material architectures that optimize the movement and recombination of charge to increase the amount of photons that emit.<sup>4-5</sup>

An organic photovoltaic (OPV) is an organic electronic device that produces current by converting absorbed light into free charge carriers. OPVs achieve this by a mechanism that broadly is the reverse of an OLED: incoming light produces an excited state on a molecule, this excited state is transferred among molecules until it reaches a species that can dissociate the electron-hole pair, and the produced charge carriers are collected. A general device structure for OPVs is shown in Figure 1.2. Some OPVs utilize separate hole and electron transport layers that also halt the transfer of the other kind of charge carrier. The most common metric OPVs is the power conversion efficiency (PCE), the ratio of the power output to the power from incoming light sources. Development of better OPV is generally focused on improving the electronic and optical response of the OSC.

The morphology of the OSC directly impacts how well charges and excited states move through the material. Generally, there are two accepted theories for how charges move through an OSC: the band regime and hopping regime. The band regime involves delocalizing the combined wavefunctions over the whole material, leading to strong electronic coupling between neighboring molecules. This coupling can be measured and is

one-fourth the size of the conduction band. Maximizing this electronic coupling decreases the time a charge carrier resides on any individual molecule to the point that transfer occurs faster than geometric relaxation, creating a delocalized transfer. Enforcing a structure that adheres to the band regime requires high order and results in high mobility, so designing materials to encourage band transfer is ideal. Since orbitals on neighboring molecules need to overlap for transfer to occur, the intermolecular behavior of the material plays a large part on the resulting conductive ability. Optimizing both the material mobility and the packing order, and thus determining a relationship between structure and electronic properties, is an open problem in the field of organic electronics.<sup>6</sup>

In contrast, the hopping regime exhibits more particle-like behavior for charge transport achieved through the coupling of electrons, molecular vibrations, and phonons, which are vibrational modes of the solid. Using the exponential Arrhenius rate law, equation (1), a relationship can be determined between the rate of the charge transfer and various energies within a molecular species undergoing electron-phonon coupling. This relationship is known as the semi-classical Marcus expression (originally derived by Rudolph A. Marcus, equation (2)), and provides considerations for how the temperature ( $T$ ), electronic coupling between final and initial states ( $H_{AB}$ ), the free energy change ( $\Delta G^0$ ), and the geometric reorganization energy ( $\lambda$ ) all impact the transfer rate ( $k_{ET}$ ).<sup>7</sup> The coupling in the hopping regime is proportional to the square-root of the Marcus-derived transfer rate, and as with the band regime, the largest material mobilities are found when the coupling is maximized. Another open problem in the field is the development of a consistent model that will unite both the hopping and band regimes, and will accurately describe when one is favored over the other.

$$rate = Ae^{-\frac{\Delta G^\ddagger}{k_b T}} \quad (1)$$

$$k_{ET} = \frac{2\pi}{\hbar} |H_{AB}|^2 \frac{1}{\sqrt{4\pi\lambda k_b T}} e^{-\frac{(\lambda + \Delta G^0)^2}{4\lambda k_b T}} \quad (2)$$

For efficient charge transport to occur, the interactions between species at interfaces must be optimized. In an OPV, these interfaces occur at the boundaries of regions of donor and acceptor species in the OSC material layer and between the OSC and the electrodes. The processing techniques used to fabricate the OSC are largely what determine the overall structure, but the chemical structure of the individual molecules also plays a role. In the OSC, two general junction types are formed: the bilayer and the bulk heterojunction (BHJ). The bilayer structure is created by depositing one material onto a substrate, and then adding the next material. While the bilayer benefits from one large consistent interface between the two types of materials, the typical diffusion length of excitons (electron-hole pairs) is around 10 nm, yet the individual layers are around 100 nm, a thickness that is required to absorb light. Thus only a fraction of excitons are able to split into charge carriers and be collected in a bilayer-OPV.

The BHJ structure, on the other hand, is much more varied. In this type of OSC structure, the donor and acceptor materials are blended together in the condensed phase. Commonly, the donor is a polymer and the acceptor is a fullerene-based species, but polymer-polymer systems and non-fullerene-acceptors are becoming more popular. The BHJ is achieved by using solutions of the two components that are cast onto a substrate and allowed to separate via annealing, after which the two species will self-assemble into a condensed mixed-phase material. Too fine a dispersion will result in poor charge transfer, but too large of domains results in the same size problems that are found in the bilayer devices. An ‘ideal’ BHJ is one that has an even distribution of each species throughout the layer, and can easily funnel the charge carriers off to their respective electrode.<sup>8</sup> Sketches of the bilayer, typical BHJ, and an ‘ideal’ or ordered BHJ are shown in Figure 1.3. While the BHJ is generally accepted to be the better morphology for polymer-based systems, determining the behavior of the acceptor and donor domains is key in future design of materials. Other work into these morphologies has investigated various treatments and processes during fabrication. One such processing effect is upon increasing the thermal annealing time for a BHJ, the size of the internal domains of donor and acceptor increase, which in turn provides more order for the system.

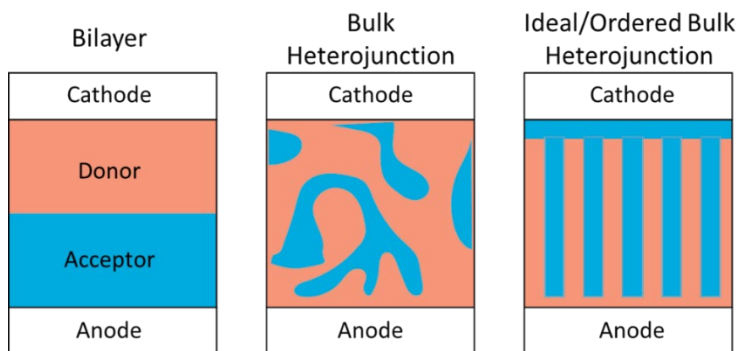


Figure 1.3: Internal structure of the OSC material in an OPV device. The donor and acceptor materials can be processed and added to the device in different ways during fabrication, resulting in different morphologies.

### 1.3 Folding and Structure of Conjugated Polymers

The internal structure of an OSC directly influences its charge-carrier ability. The morphology polymer systems are generally harder to describe than their molecular counterparts, but learning more about any relationships between the structure of the components in the monomer, the overall chain structure, and the material morphology can lead to rules for efficient design of future materials. Compared to a non-conjugated polymer, the structural dynamics of a  $\pi$ -conjugated polymer are already restricted due to the increased rigidity along the backbone, due to the fact that the main chain is comprised of planar aromatic or  $\pi$ -conjugated species. As discussed previously, the orbital overlap is crucial to charge movement along the chain, so reducing the ways the chain can bend and

fold is important. While the field of polymer-based OSC materials started with simple polymers like polyacetylene, polythiophene, and poly(p-phenylene vinylene), many of the polymers currently being developed and studied are more complex copolymers, the dynamics of which also have increased complexity.

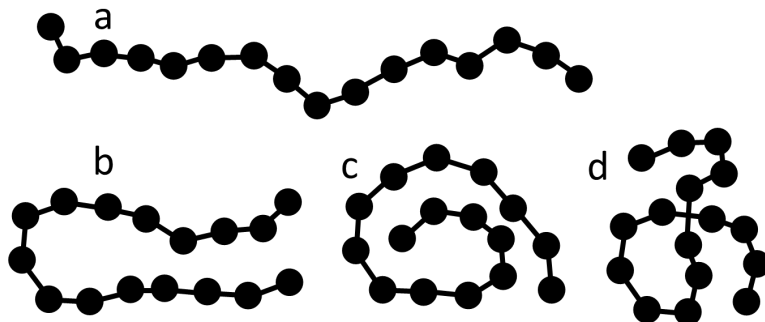


Figure 1.4: Common chain structures for  $\pi$ -conjugated polymers; a) The rod/coil shape, defined by a mostly linear chain with end points far apart; b) stacked rod conformation, with fold(s) but still largely linear; c) the toroid, identifiable with a spiral shape and some void space on the inside of the structure; d) the molten globule, which is the most disordered structure.

Common chain structures for  $\pi$ -conjugated polymers are the rod/coil, stacked rod, toroid, and globule, sketches of which are shown in Figure 1.4.<sup>9</sup> In this work, computational methods are used to simulate various  $\pi$ -conjugated polymers in the condensed phase to investigate the shapes and discern any patterns in the folding and collapsed states of the chains. Determining a mathematical model that can be used to describe the conformational state of a polymer chain given environmental parameters and chemical structures without having to view representations of the simulations would be useful, but such a model is an incredibly complex problem. However, if the influences of certain smaller molecular components can be understood, then maybe the effects of using them together can be studied. In this work, various levels of structure of the condensed-phase simulated systems are investigated to observe any relationship among the chemical, chain, and bulk structures. The shape will be related to certain physical and thermodynamic properties to provide an experimental and measurable basis by which these simulations and results can be tied to non-computational understanding.



## CHAPTER 2. COMPUTATIONAL METHODS: THEORY AND TECHNIQUES

### 2.1 Molecular Dynamics

Molecular Dynamics (MD) is a computational method that employs classical Newtonian motion to simulate systems over time, using the movement of atoms to model system evolution. The equations of motion are solved numerically over all  $N$  atoms by evaluating the forces and energies of interacting atoms, which is easier than trying to evaluate dynamic evolution analytically. The coordinates of each time step are recorded as the system evolves, which when considered as a function of time represent the trajectory of the system. Properties of interest can be determined by averaging behavior over a trajectory of a system at equilibrium.

MD is a good method for systems that can easily reach a near-equilibrium state, but it does have its limits. For one, the method is entirely classical. The contributions of hydrogen bonding, for example, are not modeled as accurately as they would be with a quantum mechanical method. Additionally, this excludes the ability to consider reactions, excited states, and more significantly, electron transfer processes. For this reason, all MD work cannot be used to make any direct conclusions about the electronic capabilities and behaviors, but can be used to observe physical phenomena of interest.

The typical simulation algorithm follows the process shown in Figure 2.1. First the positions,  $r$ , velocities,  $v$ , and interaction potential,  $V(r)$ , of all atoms in the system are used to generate an initial state. Positions and the potential are obtained from the Cartesian coordinates and the force field, while velocities are generated by using a Maxwell distribution based on the temperature of the system if not available from a previous step in the process. The next steps compute the forces on every atom with equation (3), and then update the configuration with equation (4). If necessary, the algorithm records output data. The force calculation, coordinate updating, and data output are repeated for the length of simulation time.

$$\mathbf{F}_i = -\frac{\partial V}{\partial r_i} \quad (3)$$

$$m_i \frac{\partial^2 r_i}{\partial t^2} = \mathbf{F}_i, i = 1 \dots N \quad (4)$$

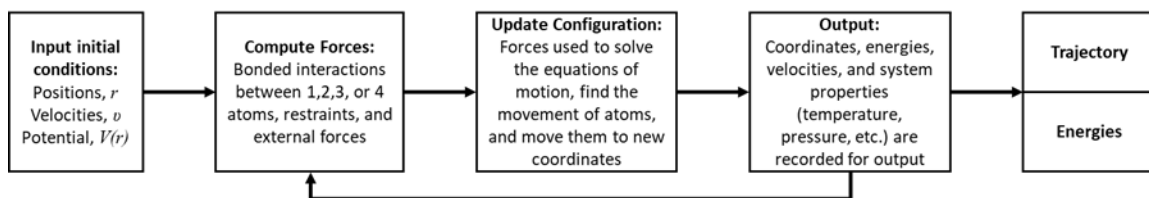


Figure 2.1: Algorithm for determining atomic movement in each step of a MD simulation. The type of simulations can vary and are discussed in section 2.2.2, but the algorithm for the motion of the atoms generally follows this procedure. Steps two through four are repeated for every time step in the simulation, which is usually 1 or 2 femtoseconds. The trajectory and the energies are used for analysis and as the initial conditions for any further simulations.

### 2.1.1 Force Fields

All of the information needed to describe the potential energy of a system in simulation is contained in a functional energy potential and parameter sets known as a force field. There are many force fields with varying applications, most being developed for different biological systems and environments, such as aqueous solution, salt solution, inner-membrane, or inner-protein. The functional form of any force field is a summation of various energy contributions of the bonded and nonbonded geometries of the system, as shown in equation (5). The bonded interactions include bond length fluctuation, bond angle fluctuation, and dihedral contributions. The nonbonded contributions come in the form of electrostatic and van der Waals attractions and repulsions.

$$E_{total} = E_{bonds} + E_{angles} + E_{dihedrals} + E_{electrostatics} + E_{van\ der\ Waals} \quad (5)$$

The bond and angle interactions take the form of harmonics that are restrained through a force constant, where the strength of the bond is directly proportional to the size of the force constant, similar to Hooke's law. These harmonics are functions of either the bond length,  $r$ , or angle,  $\theta$ , adjusted with the value of the bond or angle when all other contributions in the force field are zero,  $r_0$  and  $\theta_0$  respectively. This is different than the equilibrium bond length or angle, which would be the minimum value when all other terms are nonzero. Dihedral contributions are more complex and take the form of a summation of the first four cosine terms of a Fourier series of  $\phi$ , the angle formed from the intersecting planes of three of any four bonded atoms. All the internal coordinates for each kind of bonded interaction are shown in Figure 2.2. Nonbonded interactions are typically the most computationally expensive, and often the electrostatics term is substituted with Coulomb's law, and the van der Waals term with a Lennard-Jones potential.

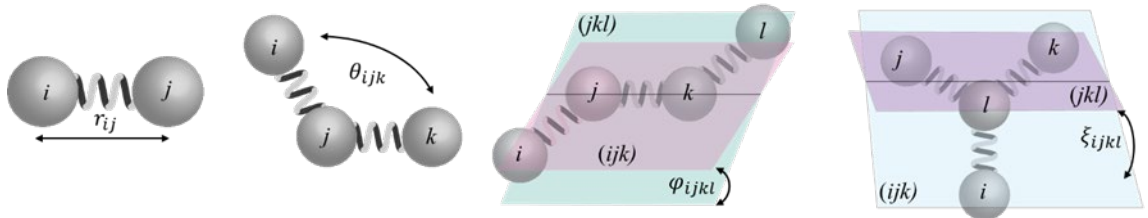


Figure 2.2: Representations of the internal coordinates for the bonded interaction terms in an interatomic potential. LEFT: stretchable bond between two atoms. MIDDLE-LEFT: Flexible angle between three atoms. MIDDLE-RIGHT: Rotatable proper dihedral angle between four consecutively bonded atoms. RIGHT: Improper dihedral angle between four bonded atoms, used to constrain planar and chiral groups.

The functional forms are made specific for each type of atom through parameter sets that connect a certain molecular environment to a force constant and minimum values. Some of these are all-atomic, meaning they include parameters for all atoms in the system. Simpler parameter sets are united-atom, which includes contributions from hydrogens in methyl or methylene groups into their parent carbons, or coarse-grained, which sums the contributions of groups of atoms into larger ‘superatoms.’ Since the parameters represent force constants in potential energy functions, the units for these parameters are  $\text{kJ mol}^{-1}$ .

This work uses the all-atom Optimized Potentials for Liquid Simulations Force Field (OPLS-AA), developed by William Jorgensen and co-workers.<sup>10</sup> This force field was optimized for experimental properties of liquids and gas-phase torsional potentials. This allows the use of gas-phase simulations to obtain data about macroscopic structural behavior and to simulate conjugated organic systems in their liquid and amorphous environments. The functional form of OPLS is similar to many others, specifically AMBER, both of which deviate from the general functional form by combining the electrostatics and van der Waals terms into one  $E_{nonbonded}$  term that only considers atoms that are more than three bonds apart to reduce breaking bonds due to strong Lennard-Jones repulsions.<sup>11</sup> This nonbonded energy is scaled by a ‘fudge factor’ of  $f_{ij} = 0.5$  for 1,4 interactions for the same reason, but is not scaled for atoms further than four bonds apart ( $f_{ij} = 1$ ). The functional forms of all energy terms are shown in equations (6) through (9).

$$E_{bond}(r_{ij}) = \sum_{bonds} K_b (r_{ij} - r_{ij,0})^2 \quad (6)$$

$$E_{angle}(\theta_{ijk}) = \sum_{angles} K_\theta (\theta_{ijk} - \theta_{ijk,0})^2 \quad (7)$$

$$E_{torsions}(\varphi_{ijkl}) = \sum_{torsions} \frac{1}{2} \sum_{n=1}^4 C_n (1 + (-1)^{n-1} \cos(n\varphi)) \quad (8)$$

$$E_{nonbonded}(r_{ij}) = \sum_{i=1}^{N-1} \sum_{j=1+1}^N f_{ij} \left\{ 4\epsilon_{ij} \left[ \left( \frac{\sigma_{ij}}{r_{ij}} \right)^{12} + \left( \frac{\sigma_{ij}}{r_{ij}} \right)^6 \right] + \frac{q_i q_j e^2}{r_{ij}} \right\} \quad (9)$$

MD software is typically designed to simulate biological systems: proteins, lipids, and nucleic acids, so any non-biological molecules and uncommon solvents have to be added to the force field.<sup>12</sup> Conveniently, the parameterization of biologically-relevant components is taken from experimental data and quantum mechanical calculations of similar small-molecule organic species, so parametrizing small organic systems is well within the typical practice. The process of parameterization of new molecules starts with using a lowest-energy optimized structure from which various geometric properties of interest are modified to generate a potential energy surface that is fit to the functional form. For most organic systems, the values for bonds and angles are consistent among molecules with similar molecular environments and can be transferred between species without significant error, reducing the number of calculations need to parameterize new molecules. For example, if benzene has been fully parameterized, then phenyl groups have been parameterized except for at the new attachment point. Any bonds or angles that do need entirely unique parameters can be obtained by modifying the bond of angle length and fitting the resulting energy landscape to the appropriate harmonic.

Of higher importance to the materials studies in this work is the accurate modeling of dihedral potentials, which must be obtained through rigorous calculation for all new rotational environments, despite their similarity to existing parameters, as to properly model the expected rotational configurations. The rotational potential energy surface is obtained by optimizing the ground state energy for different angles of the dihedral of interest. For symmetric dihedrals, like the linking bond in 2,2'-bithiophene, only 180° of the potential has to be calculated as 181° would be geometrically equivalent to 179°. For antisymmetric dihedrals (usually caused by side chains, not elements in the backbone), the full 360° is scanned. The 'smoothness' of the obtained potential is indirectly proportional to the step size, but a smaller step size increases the number of steps required and thus increases the computational cost. For this reason, it is common to use steps of 10° each, with 18 or 36 steps depending on the length of scan needed. The parameterization for OPLS uses the Ryckaert-Belleman function, equation (10), as a simplification for fitting the dihedral potential. Using this version of the dihedral to obtain parameters and then convert them to the Fourier form is more efficient than fitting the Fourier terms. This is the parameterization for proper dihedrals, which is the dihedral angle for four consecutive atoms in a chain. The dihedral angle for any four non-consecutive atoms is known as improper, as seen in Figure 2.2, and can be described with the same functional form as the proper dihedrals or with a harmonic potential. OPLS uses a harmonic similar to the bond and angle functions, as shown in equation (11). Improper dihedrals are of great importance to modeling organic electronic systems, as they are fit to enforce planarity in aromatic and conjugated groups or to prevent chiral flipping.

$$V(\{r\}) = \sum_{n=0}^5 C_n \cos^n(\psi), \psi = \varphi + 180 \quad (10)$$

$$V_{improper}(\xi_{ijkl}) = \frac{1}{2} K_{\xi} (\xi_{ijkl} - \xi_0)^2 \quad (11)$$

The parameters for the nonbonded energy ( $\sigma_{ij}, \epsilon_{ij}$ ) are also often easily transferrable between similar molecular environments. Partial charges however, are much more finely tuned. Partial charges are tuned to create groupings of atoms that give a partial charge sum of zero. Typically all parameters are obtained with quantum mechanical methods to achieve the most accurate ground-state geometries possible. Density Functional Theory, the method used for obtaining parameters of the systems in this work, is discussed in section 2.2

### 2.1.2 Simulation Workflow

Accurately simulating a molecular system requires a number of steps to achieve a state that is representative of equilibrium. Firstly, after generating the initial coordinates of the system by creating a simulation space and inserting molecules where desired, the system is run through an energy minimization (EM) step to minimize the forces on all of the atoms. This step is not specifically a MD simulation, but is included here as part of the overall workflow of system setup. EM steps are performed using either a steepest descent or conjugate gradient algorithm, both of which apply forces to atoms and accept a new position based on a threshold test for scalar force, similar to a Monte Carlo algorithm. All following steps are some variety of statistical ensemble, with constant number of atoms, and temperature,  $N$  and  $T$ , plus either constant volume,  $V$ , or pressure,  $P$ , termed the NVT and NPT ensembles respectively. NVT steps allow for configurational sampling without changing the volume of the system or for large changes in temperature without trying to restrain the pressure. In comparison, NPT steps are used from system compression and for making predictions of real-world properties, as the NPT ensemble most closely resembles an experimental setting. Temperature, pressure, and many other system properties are controlled through their own algorithms and constraints that are set when the simulation is generated.

A thermostat is an algorithm designed not to force the temperature during a simulation to be constant, but to keep the average temperature of the simulation within an acceptable range. If the temperature were to be held constant then there could be no change in the total kinetic energy, thus defeating the point of using NVT or NPT. Rather, allowing fluctuations in the atoms' kinetic energies and averaging over the kinetic energy of every atom results in an average temperature with deviation decreasing as the number of atoms increases. The activation of this function is attached to the simulation time via a coupling constant in units of time. All of the simulations in this work use the canonical velocity-rescaling Berendsen thermostat to ensure that a canonical ensemble is maintained by coupling the system to a heat bath at the desired temperature and minimizing the fluctuations.<sup>13-15</sup>

Corrections to the pressure are maintained by similar algorithm to thermostats, appropriately known as barostats. If there is no pressure coupling involved, then the system size stays constant, similar to true NVT. Pressure is important for the calculation of thermodynamic properties, so controlling its fluctuations is crucial. The Berendsen and the Parrinello-Rahman barostats are used in this work, which both operate in similar fashion to the heat bath in the thermostats, but with a constant that constrains pressure at certain

time steps.<sup>16</sup> Additionally, an extra degree of freedom is added and the Hamiltonian for the motion of particles is extended, allowing for a closer approximation of the true NPT ensemble.

The geometry of the simulation space is another aspect that can be manipulated, and the shape and properties chosen can yield significant differences in system evolution and calculated outputs. The three-dimensional shape of the simulation takes the form of either a cubic/rectangular prism, triclinic box, truncated octahedron, or a rhombic dodecahedron. Certain shapes are better for certain systems, e.g. water molecules can easily get ‘stuck’ in the corners of a prismatic space, so the truncated or rhombic spaces are best for simulations with a large amount of solvent. Along with the system shape, the behaviors at the boundaries can also be manipulated. The most common treatment is to use periodic boundary conditions (PBC) in all three Cartesian directions. This allows for the atoms that move out of the simulation space in one direction to appear in the space on the opposite side of the box while maintaining their momentum. This is interpreted as a perfect repeat of the simulation space existing nearby and that the exit of the system’s atoms is matched by the entering of a copy’s atoms. As a result, surface effects are also removed, since PBC is repeated *ad infinitum* and therefore there are no free surfaces. PBC can be applied to all directions of motion, or be combined with walls and restricted to two dimensions. These walls act as hard boundaries for the system and can be customized to behave in different ways.

The treatment of nonbonded interactions can also be manipulated within the simulation parameters. For the van der Waals interactions, a cut-off of approximately 10 Ångstroms is sufficient to capture the behavior of the Lennard-Jones potential that the functional form uses as the interaction decays quickly as interatomic distance increases. For the electrostatics term, the Coulombic term decays slowly with distance, thus allowing the potential to take effect over long distances. Thus a cut-off scheme to decide when electrostatic interactions need not be considered is required to reduce computational cost. The Particle Mesh Ewald (PME) cut-off method splits the entire electrostatics calculation into the sum of two terms: a short-range potential in real-space and a long-range summation in Fourier space.<sup>17</sup> Both summations converge quickly in their respective spaces, so the treatment uses low computational cost. A periodicity assumption is made in PME, requiring PBC.

The last parameters of note are the constraints and restraints put in place during a simulation. Constraints are used to restrict the length of bonds and angles after the integration of forces. This works uses LINCS (Linear Constraint Solver), which is a fast method that corrects the bond lengthening due to unconstrained updates.<sup>18</sup> The algorithm works in two steps: one to figure out the forces that moved the atoms in a bond to an unfavorable length, and then uses the pre-image of the bond to correct the length within accordance to the forces that cause the unconstrained geometry. Restraints are used to impose restrictions on the movement of the system by incurring a large change in the potential energy if a certain geometric change occurs. Restraints can be used to restrict complete positional displacement, bond lengths, angles, and dihedral rotations.

All of these simulation parameters are used to generate different types of simulations that move a system from initialization to equilibration. Achieving equilibration

follows some common steps that are customized for each system. After the initial coordinates are generated and the forces on all atoms are minimized to a desired value, the system goes through various heating and compression stages to achieve the desired level of equilibrium. The number of steps, the order, and each step's length vary among procedures and the types of systems being simulated. For polymers, previous work has shown that using an annealing process that fluctuates between room temperature and some elevated temperature, and various level of compression, using alternating NVT and NPT steps, and applying complete positional restraints for early parts of the process results in a system that is much closer to a realistic equilibrium state of a material rather than allowing for a system to collapse simply at room temperature. Once the system has reached equilibrium, which is typically tracked through the deviation in the potential energy or specific measured properties such as the density, all further MD simulations are considered 'production steps,' which is where data is obtained.

All molecular dynamics simulations in this work are performed with the GROAMCS 2019 software suite.<sup>19-21</sup> The force field used is OPLS-AA, as discussed in this chapter. Specific simulation setup, steps, and unique procedures are discussed the respective methods sections 3.2 and 4.2.

## 2.2 Density Functional Theory

Density functional theory (DFT) is quantum-mechanical approach to evaluate the energy of many-body systems through the use of functionals (a function of functions) of the electron density. Since the focus of the simulations in this work is on the macroscopic behaviors of polymer chains and their morphologies through MD approaches, DFT is used only to obtain ground-state optimized structures, and to parametrize systems for use in MD simulations. All parameterization via DFT in this work was performed with the Gaussian 16 Rev. A. 03 suite.<sup>22</sup> Ground-state energy optimization and dihedral scans were performed with the 6-31G(d) split-valence basis set and the  $\omega$ B97XD functional.<sup>23,24</sup> Dihedral potentials are obtained through the process described in section 2.1.1, and partial charges are obtained using the charge model 5 (CM5) framework.<sup>25</sup> For the non-fullerene acceptors, charges are obtained from optimizing the singular structure. For the polymers, three different sets of partial charges are generated for an inner monomer unit and the two end units. These charges are fixed to make sure these units give an overall zero sum no matter the number of units in the chain.

## CHAPTER 3. DISRUPTING THE BACKBONE $\pi$ -CONJUGATION IN DPP-BASED POLYMERS

### 3.1 Introduction

As discussed in section 1.3, the most efficient charge transfer in polymer-based organic semiconducting systems is reliant on rigid  $\pi$ -conjugated backbones. Varying the donors and acceptors in the polymer is a common method of searching the chemical space for possible species of interest.<sup>26</sup> Another way in which the backbone can be altered is to purposefully disrupt the conjugation by adding alkyl-based fully  $sp^3$ -hybridized segments known as conjugation break spacers (CBS) into the monomer structure. While this removes the ability to transport charge along the entire length of the chain, the overall flexibility of the polymer is increased, resulting in different folded structures compared to the fully  $\pi$ -conjugated variety. This increase in flexibility and folding capabilities leads to more robust mechanical properties and good mobilities, based on intermolecular hopping-type transport, when the new polymers are used to create thin films or are blended with a small concentration of the fully-conjugated variety.<sup>27</sup>

This work investigates the effects of introducing a linear CBS segment ranging from one to ten methylene units into diketopyrrolopyrrole-tetrathiophene polymer [DPP-4T], the structure of which is shown in Figure 3.1. The notation DPP-m is used to denote the CBS moieties, from DPP-1 to DPP-10. Diketopyrrolopyrrole [DPP] pigments have been shown to be great acceptors and the polymers that utilize DPP as an acceptor unit show low band gaps and high mobilities. Janssen et al. showed that a polymer composed of alternating DPP and terthiophene units resulted in a band gap of 1.3 eV with electron and hole mobilities of 0.01 and 0.04  $\text{cm}^2/\text{V sec}$ , respectively, in OFET devices.<sup>28</sup> Single-component systems of DPP-4T and DPP-m are investigated for local structure and condensed-phase morphology, as well as thermal properties. In addition, systems of fully  $\pi$ -conjugated DPP-4T in a blend of DPP-m are observed for variations in the condensed morphologies.

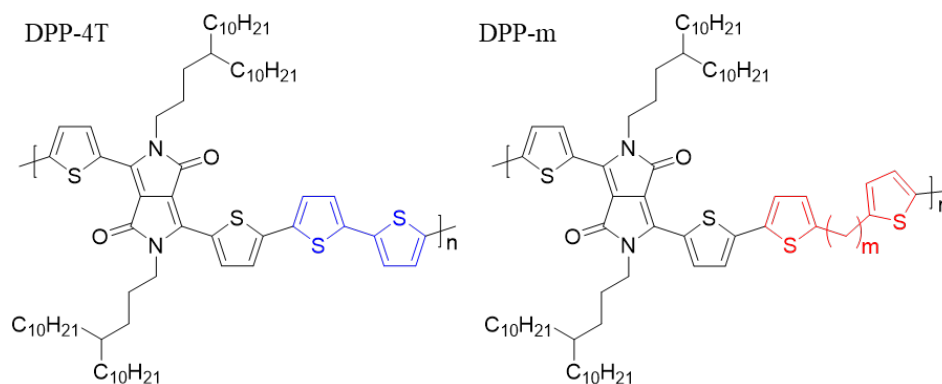


Figure 3.1: Structures of DPP-4T and DPP-m. The CBS unit ( $m$ ) ranges from 1 to 10 carbons in length.



## 3.2 Methods

Details regarding the force field implementation and software used follow the discussions in Chapter 2. Three types of systems were simulated for these experiments: a single-chain vacuum system, single-component bulk of 20 chains of all 11 polymers, and multi-component bulk wherein a single DPP-4T chain is mixed in 19 DPP-m chains. All DPP-4T chains consist of 20 repeat units, and all DPP-m chains consist of 10 repeat units. The number of atoms and the weights of each chain are listed in Table 3.1. These values are consistent with the  $M_n$  and dispersity indices (DI) of those synthesized in Reference<sup>29</sup>. Experimental  $M_n$  for DPP-4T is 30.7 kDa with a DI of 3.6 and the DPP-m range from  $M_n$  of 6.6 to 15.4 kDa and DI that range from 1.2 to 1.4, with  $M_n$  generally increasing as the CBS increases.

Table 3.1: Atom counts and weights for the DPP-4T and DPP-m polymer chains.

polymer	atom count	$M_n$ (kDa)
DPP-4T	3682	22.719
DPP-1	1872	11.500
DPP-2	1902	11.641
DPP-3	1932	11.781
DPP-4	1962	11.921
DPP-5	1992	12.061
DPP-6	2022	12.202
DPP-7	2052	12.342
DPP-8	2082	12.482
DPP-9	2112	12.622
DPP-10	2142	12.763

The vacuum simulations were initialized by randomly inserting an extended polymer chain into a simulation box large enough to ensure that the polymer is at least 2 nm away from any box edge and 4 nm away from any replicate upon rotation. Parallel simulations were thus run with slightly differing initial configurations. Each system was treated with an initial energy minimization using the conjugate-gradient method (force on atoms <1000 kJ/mol/nm) followed by an NVT simulation at 300 K for 2 ns, during which the collapse of the polymer chains from extended to folded was observed. This was repeated three times to generate three separate folding trajectories. The NVT simulation used a leapfrog integrator with a 1 fs time step, the velocity rescaling thermostat with 0.1 ps coupling constant. The short-range cutoff was 1.4 nm and long-range interactions were treated with PME summation. Initial velocities were assigned with a Maxwell distribution at 300 K and all hydrogen bonds were constrained with the LINCS method. Section 2.1.2 includes detailed explanations of these algorithms.

The bulk-phase simulations follow the same initialization, equilibration, and production simulations for the single- and multi-component systems, with an extra

equilibration for the single-component system which generated a lower temperature configuration to use for thermal analysis. All systems were initialized by randomly inserting 20 polymer chains in a simulation box and ensuring there was no polymer overlap. The systems were then compressed and decompressed through a series of NVT and NPT steps as outlined in Table 3.2 to generate the initial room temperature glass models. For the single-component systems, additional steps were used to generate initial configurations at 100 K for a temperature ramp up to 800 K at steps of 100 K that followed a repeating scheme of 10 ns NPT equilibration, 2 ns NPT at the new temperature using the coordinates from the previous equilibration, and then another 10 ns equilibration. Unless specifically noted, all temperature-independent analysis and production steps were performed on systems at 300 K.

Table 3.2: Compression and decompression steps for the condensed-phase systems.

<b>step</b>	<b>conditions</b>	<b>duration (ns)</b>
1	NVT 550 K	2
2	NVT 300 K	2
3	NPT 1000 bar, 300 K	2
4, 5	NVT 550 K, NVT 300 K	1,2
6	NPT 2500 bar, 300 K	2
7, 8	NVT 550 K, NVT 300 K	1,2
9	NPT 1000 bar, 300 K	2
10, 11	NVT 550 K, NVT 300 K	1,2
12	NPT 500 bar, 300 K	2
13	NVT 300 K	2
14, 15	NPT 1 bar, 300 K	2,10
16	NPT 1000 bar, 100 K	2
17, 18	NVT 300 K, NVT 100 K	1,2
19	NPT 1 bar, 100 K	2,10

The NPT compression steps all used a temperature coupling constant of 0.1 ps and a velocity rescaling thermostat and a pressure coupling constant of 2 ps with the Berendsen barostat. Equilibration and production NPT steps use the Parrinello-Rahman barostat. Positional restraints are enforced to prevent polymer self-solvation through step 14 as detailed in Table 3.2. The hydrogen bonds are again constrained with the LINCS algorithm. Following equilibration, a 10 ns NPT simulation is used to generate the trajectories that will be analyzed. All steps were completed in triplicate to generate three unique configurations and trajectories for each type of system.

### 3.3 Results and Discussion

#### 3.3.1 Vacuum Simulations

The vacuum simulations were performed to provide insight as to how the introduction of the CBS influences the folding of the polymer chain during self-solvation in poor solvent. All chains started in an extended state such that the end-to-end length was similar to the contour length of the polymer. The simulations ran for 2 ns, during which coordinates were recorded every picosecond such that 2000 configurations were obtained for one collapse trajectory. Since this was repeated in triplicate, 6000 configurations were obtained for each of the 11 polymers. Figure 3.2 shows the average radius of gyration ( $R_g$ ) as a function of time over three unique simulations for the first 300 ps of simulation. After 300 ps, there was no discernible change in  $R_g$  for any of the 11 polymers. The  $R_g$  of the chains at the beginning and end of the simulation are listed in Table 3.3, showing the values for the fully extended and collapsed structures. It should be noted that despite the longer contour length, the value for DPP-3 is lower than that of DPP-2 due to a kink in the starting structure that occurred during energy minimization. The overall trend for these two moieties with respect to each other and the collapse trends exhibited by all the polymers is unaffected. In the poor solvent that is vacuum, each polymer chain quickly self-solvates and collapses to form a globule-like shape. Even with the wide range of extended lengths at the beginning, all DPP-m chains collapse to a range of 1.33-1.37 nm, while the more rigid DPP-4T only collapses to 1.74 nm.

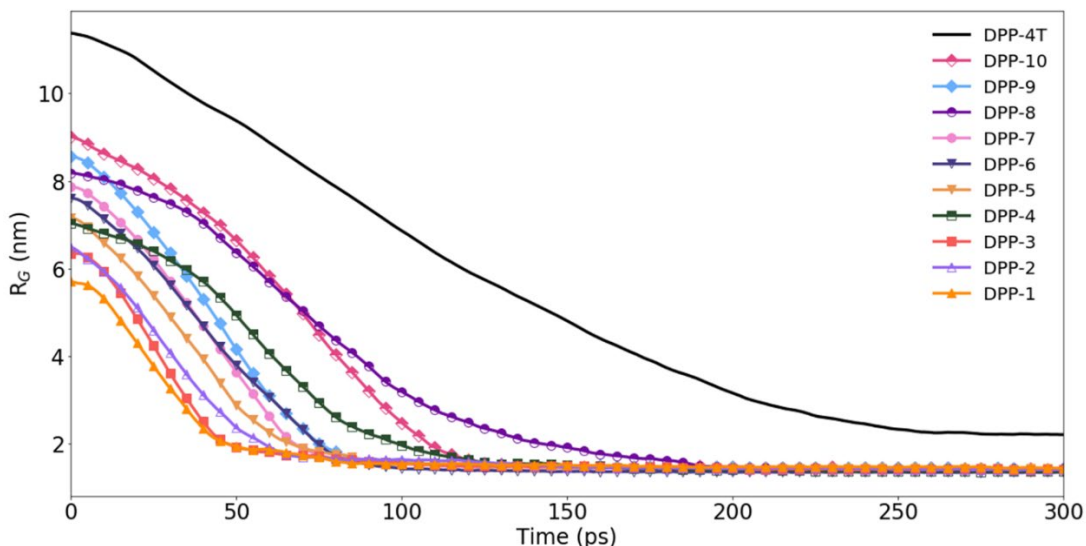


Figure 3.2: Radius of gyration (nm) versus time (ps) for the collapse of all DPP-based polymers in vacuum. The solid black line shows the behavior of DPP-4T and the colored lines with symbols represent the DPP-m moieties.

Table 3.3: Start and end values of the radius of gyration for the collapse trajectories.

polymer	Starting $R_g$ (nm)	Final $R_g$ (nm)			
		run 1	run 2	run 3	average
DPP-4T	11.376	1.687	1.735	1.794	1.739
DPP-1	5.705	1.382	1.408	1.309	1.366
DPP-2	6.48	1.354	1.359	1.369	1.361
DPP-3	6.349	1.371	1.317	1.356	1.348
DPP-4	7.029	1.333	1.325	1.339	1.332
DPP-5	7.165	1.366	1.346	1.307	1.340
DPP-6	7.615	1.320	1.328	1.345	1.331
DPP-7	7.871	1.378	1.312	1.302	1.330
DPP-8	8.187	1.409	1.323	1.309	1.347

Experimental results have shown definite trends concerning the parity (odd or even) of the CBS length used. A similar trend appears in the collapse trajectories of these DPP-based polymers. It is apparent from Figure 3.2 that the self-solvation of the fully  $\pi$ -conjugated and more rigid DPP-4T proceeds differently from the various DPP-m moieties. For DPP-4T the shape of the data indicates a longer and consistent folding process, i.e. the slope is regular between the extended and the globule-like regions. In contrast, the DPP-m species all show a steeper slope between the extended and globule-like regions than DPP-4T. Additionally, the DPP-m moieties show a longer lifetime for the extended conformation. The slopes ( $R_g$  vs time, nm/ps) of the linear region of each of the DPP-m average trajectories are listed in table 3.4. As observed in Figure 3.2 and Table 3.4, the rate of collapse for the even moieties is generally slower than that of the odd moieties. Additionally, as seen in Figure 3.3, the spread of these individual trajectories is increased for the even moieties compared to their odd counterparts, and even more so specifically for DPP-4 and DPP-8. DPP-1 also shows distinct behavior as evident by the shoulder-like region at 50-100 ps that does not appear in any other DPP-m trajectories; this behavior may be the result of DPP-1 having a more restricted range of dihedral variability.

Table 3.4: Collapse rate in nm/ps of single polymer chains in vacuum.

polymer	collapse rate (nm/ps)				
	run 1	run 2	run 3	ave.	$\sigma$
DPP-4T	-0.0484	-0.0394	-0.0476	-0.0451	0.0050
DPP-1	-0.1085	-0.0923	-0.0988	-0.0999	0.0082
DPP-2	-0.1031	-0.0840	-0.0935	-0.0935	0.0096
DPP-3	-0.1063	-0.1172	-0.1226	-0.1154	0.0083
DPP-4	-0.0838	-0.0680	-0.0907	-0.0808	0.0116
DPP-5	-0.1063	-0.0983	-0.0859	-0.0968	0.0103
DPP-6	-0.0870	-0.0839	-0.0829	-0.0846	0.0021
DPP-7	-0.0955	-0.1067	-0.1049	-0.1024	0.0060
DPP-8	-0.0450	-0.0817	-0.0713	-0.0660	0.0189
DPP-9	-0.1092	-0.0890	-0.1236	-0.1073	0.0174
DPP-10	-0.0752	-0.0797	-0.1068	-0.0872	0.0171

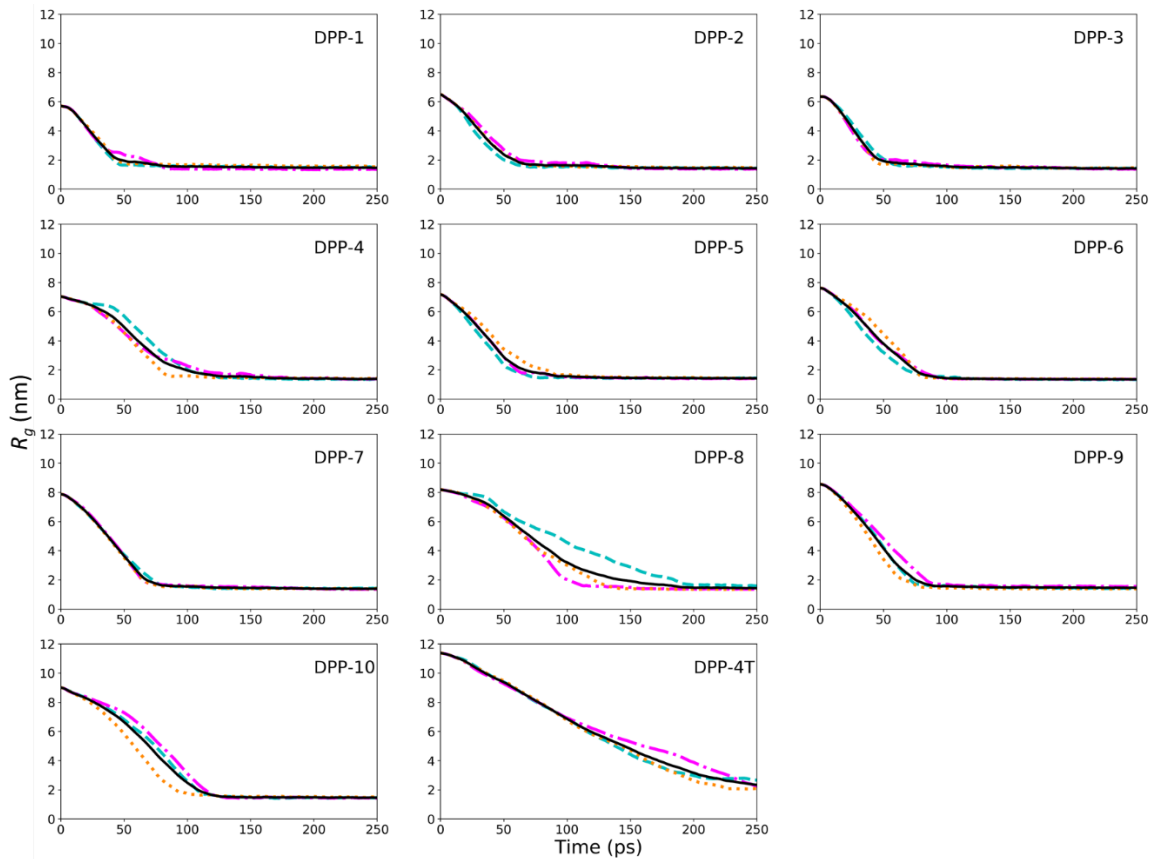


Figure 3.3: Radius of gyrations versus time for all DPP-m collapse trajectories. Individual trajectories are shown in dotted orange, cyan, and magenta lines while the average behavior is shown as a solid black line.

To better describe the evolution of these chains during the self-solvation process, attention is now turned to the structure at multiple locations along the chain. To be able to analyze all chains simultaneously, a structure that is present in every chain is chosen. Thus two analyses are performed: distributions of the dihedral angles formed by the thiophene rings that cap the CBS units and an analysis of the evolution of the vectors of the more rigid segments, i.e. the thiophene-thiophene-DPP-thiophene-thiophene repeats in-between the CBS insertions. This choice for analysis also allows for direct comparisons to DPP-4T. Figures 3.4 and 3.5 show the dihedral angle distributions for the sulfur-carbon-carbon-sulfur angle in DPP-4T and the DPP-m moieties respectively. For DPP-4T, this distribution reflects the potential that was used to parameterize the dihedral for use in MD simulation. In contrast, the angle distribution for the DPP-m chains is not a proper dihedral, but instead grants more information about the three-dimensional structure reflecting the kinking of the CBS unit. For both figures,  $180^\circ$  represents the *trans*- conformation as per the standard convention and the data points represent the fraction of time in the whole simulation that whole angles are present across all monomer units.

Similar to the  $R_g$  versus time, a trend appears in the odd and even DPP-m species. Figure 3.5 shows that the odd-length DPP-m species have a local maximum at  $180^\circ$ , similar to what is seen in DPP-4T. On the other hand, the even-length CBS, particularly DPP-4 and DPP-6 show two local maxima that border the central maxima seen in DPP-4T. As would be expected from the increase in flexibility, the distributions broaden as the CBS unit lengthens, indicating a shift towards a more even occurrence of all possible conformations. Again, DPP-1 stands out as not only the most consistent among the different trajectories, but also that it is an odd-length DPP-m with the characteristic double peaks seen in the even-length DPP-m.

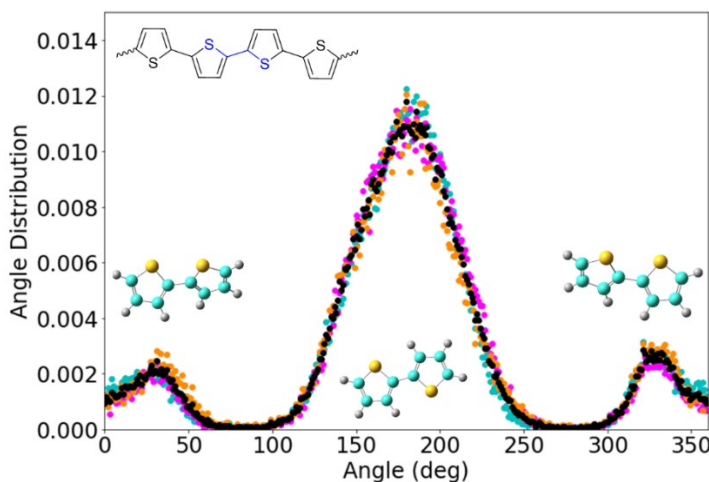


Figure 3.4: Dihedral angle distribution for the sulfur-carbon-carbon-sulfur dihedral angle between the thiophene rings in DPP-4T (highlighted on the inset structure). Bithiophene structures are representative of the angles are  $-150^\circ$ ,  $0^\circ$ , and  $150^\circ$ .

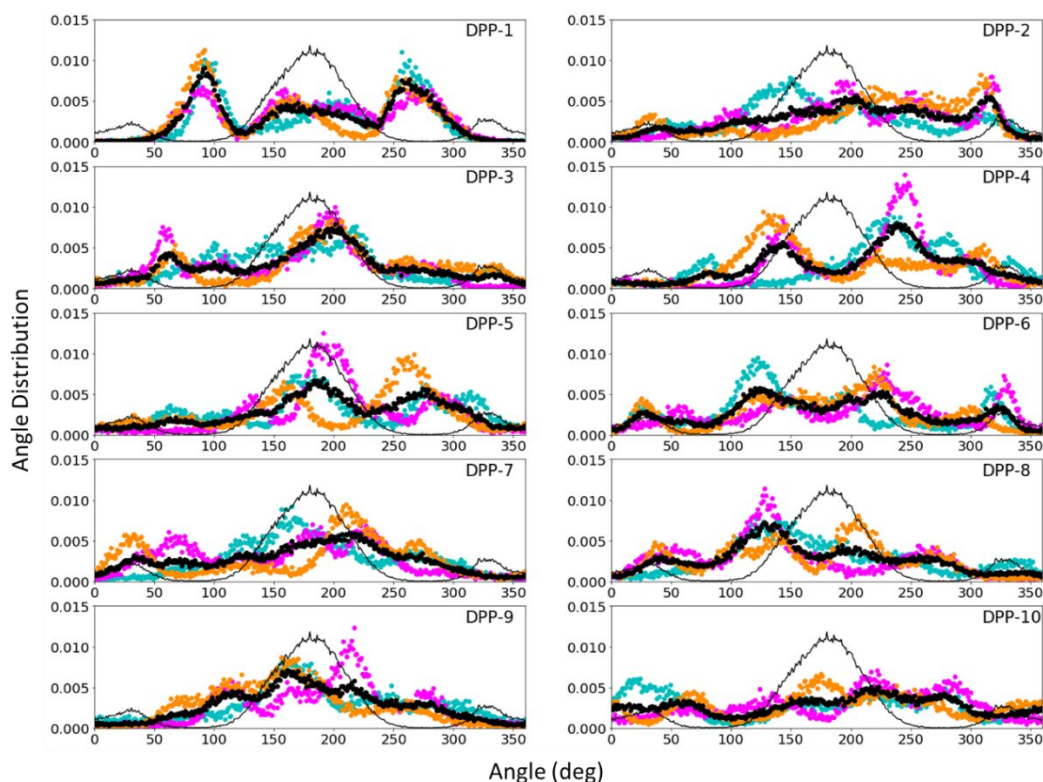


Figure 3.5: Sulfur-carbon-carbon-sulfur angle distributions for the DPP-*m* moieties. The distributions from individual trajectories are shown in cyan, orange, and magenta. The solid black dots represent the average behavior of the distributions and the solid black line is the average distribution for DPP-4T, provided for comparison.

From these simulations it is clear the single methylene unit in DPP-1 greatly restricts the available conformations of this inter-thiophene angle, and thus likely is the cause for constricting the chain and causing off-trend behavior in the  $R_g$  data as well. Additionally, the even-length DPP-*m* moieties tend to have higher variance in a preferred bending angle in the CBS segment as well as slower rates of self-solvation when compared to their odd counterparts.

### 3.3.2 Condensed-Phase Simulations

The glass models of DPP-4T and DPP-*m* species were used to determine the thermodynamic behavior in addition to morphology and folding trends. Two types of glasses were simulated: a 20-chain single-component bulk for each of the 11 polymers, and a multi-component that consists of one DPP-4T chain in 19 DPP-*m* chains. Figure 3.6 and Table 3.5 show the densities at 300 K for the single-component glasses of all species. It is seen that there is a linear trend in the density as the length of the CBS increases. The expected trend would be for the density to increase with CBS length as each successive DPP-*m* adds 30 new atoms to the monomer structure, but this trend concludes that the

volume gained by these additions overcomes the mass added, thus decreasing the density. This follows the trends in the  $R_g$  from the vacuum simulations, as longer CBS lengths led to slightly larger globule-like structures. These simulations can be considered a good representation of the system given their similarity to the density of other conjugated polymers such as poly(3-hexylthiophene) [P3HT]<sup>30</sup> at 1.1 g/cm<sup>3</sup> or the benzodithiophene-thienothiophene donor-acceptor copolymer PTB7<sup>31</sup> at 1.17 g/cm<sup>3</sup>.

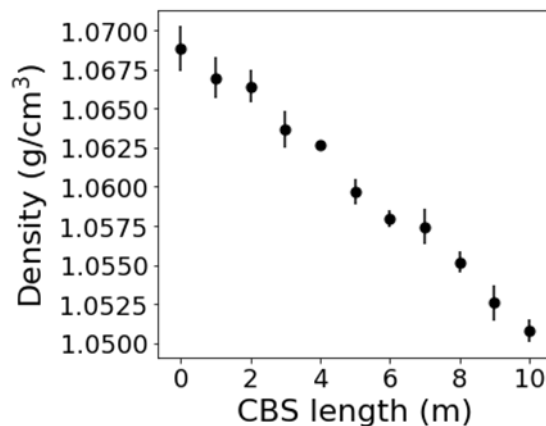


Figure 3.6: Density (g/cm<sup>3</sup>) at 300K as a function of increasing CBS length (m from DPP-m), with m=0 representing DPP-4T. Bars here represent the standard deviation from averaging over triplicate systems.



Table 3.5: Average densities for the single-component glass systems.

<b>polymer</b>	<b>average density (g/cm<sup>3</sup>)</b>	<b><math>\sigma</math></b>
DPP-4T	1.06944	0.00132
DPP-1	1.06807	0.00063
DPP-2	1.06699	0.00018
DPP-3	1.06474	0.00124
DPP-4	1.06387	0.00031
DPP-5	1.06050	0.00105
DPP-6	1.05917	0.00137
DPP-7	1.05710	0.00304
DPP-8	1.05581	0.00095
DPP-9	1.05368	0.00072
DPP-10	1.04845	0.00138

Along with the density of the glasses, thermal transitions can be probed by moving a system through a series of equilibration steps at increasing temperatures, mimicking the process of performing differential scanning calorimetry on a sample. This procedure was performed for the single-component systems from 100 K to 800 K at steps of 100 degrees, the density was extracted at each step. The following density versus temperature plots, shown in Figure 3.7, are used to predict a transition temperature, in this case the glass transition,  $T_g$ . Finding  $T_g$  from these plots involves fitting a linear fit to two subsets of the data, for all possible subsets with one side having at least two data points to fit the curve. The sum of the two linear regression R-squared values is used to assess the fit, as such the best fit has a sum-of-R-squared closest to 2.0. The temperature value that corresponds with the intersection of best fit regression lines is the transition temperature. Experimental work has shown another odd versus even pattern in melting temperatures for CBS from length of 2 to 11, then constant decrease in the temperature as the length of the CBS unit increases. It is common in computational work for the glass transitions to be over-estimated due to simulations using much faster temperature scaling, so these values are solely reported to analyze the trend, not for accuracy in prediction. Given the low variation in densities for these glasses, it is not surprising that the glass transition temperatures do not produce a wide range of values, with exceptions of systems DPP-1 and DPP-5. DPP-1 has been shown to be an exception to trends thus far, so its unique behavior here may be realistic. Altogether, this suggests that the CBS length has little effect on the thermal characteristics in these amorphous phases.

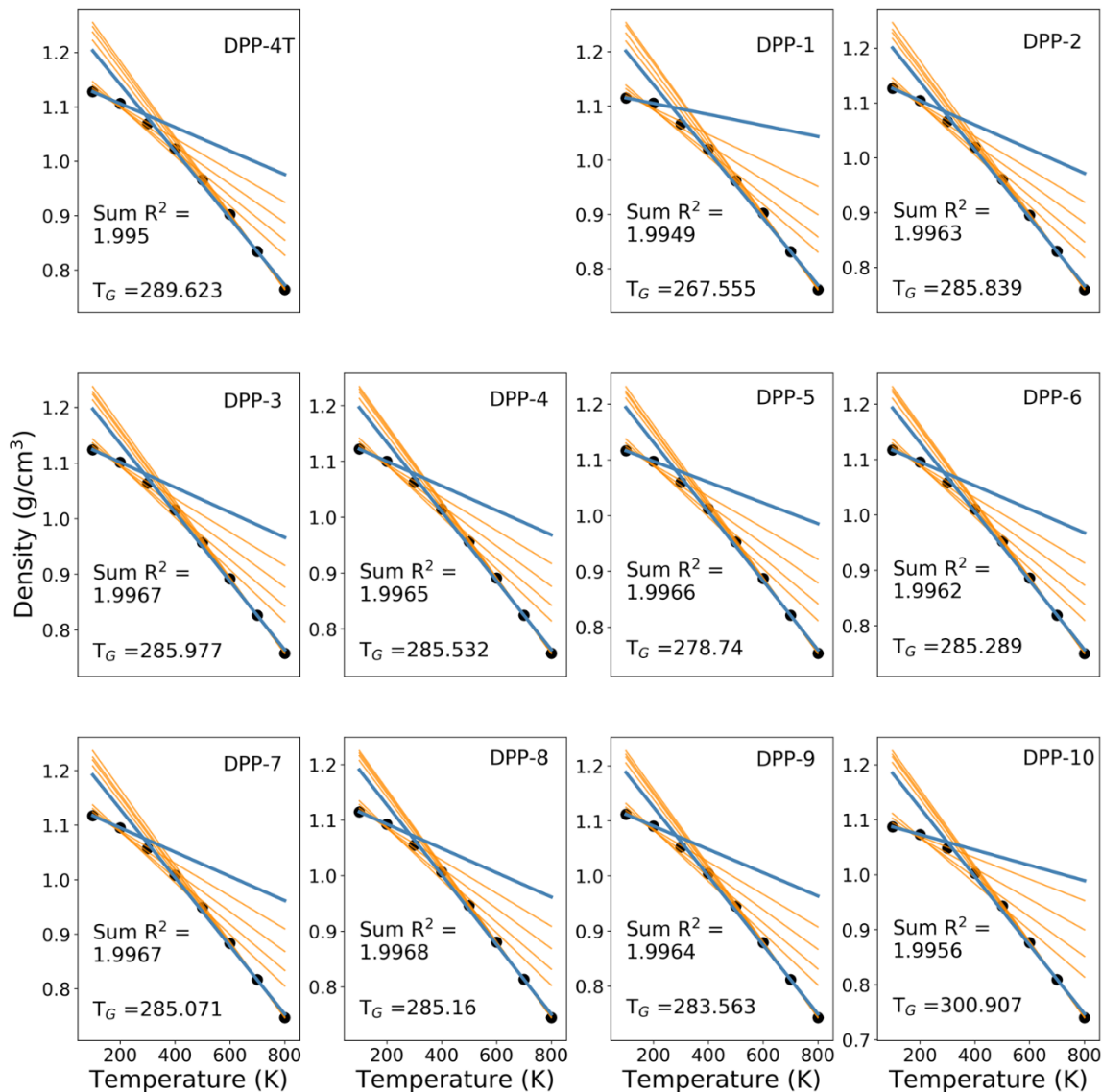


Figure 3.7: Determination of the glass transition temperature by fitting the density versus temperature data for each single-component system. Data points represent average density over three trajectories. The best fit is shown in dark blue with the sum of R-squared and the corresponding glass transition reported. All other fittings are shown in orange.

Another thermodynamic property of interest is the self-diffusion of these polymer chains in the bulk environments. The mean-squared displacement (MSD) self-diffusion constants are listed in Table 3.6 for the amorphous phase (300K) and the melt phase (600 K). As expected, the diffusion is at least a magnitude of difference larger at the elevated temperature. At 300 K, values for diffusion are larger for the even-numbered DPP-m species than the odd-valued species that are one carbon lesser. This behavior is lost at 600 K, but in general the diffusion increases with increasing CBS length, suggesting that the increased flexibility may allow for easier movement through the condensed material.

Additionally, longer CBS lengths space the alkyl side chains further apart, potentially decreasing how often different instances of the side chains interact with each other on one polymer chain. The effects of alkyl chains are not investigated in this work, but the diffusion may be tied to the intra- and inter-chain behavior of the side chains.

Table 3.6: MSD-derived self-diffusion coefficients ( $\text{cm}^2/\text{sec}$ ) for the single-component systems at 300 and 600K.

polymer	300 K		600 K	
	D ( $\text{cm}^2/\text{sec}$ )	$\sigma$	D ( $\text{cm}^2/\text{sec}$ )	$\sigma$
DPP-4T	$2.033 \times 10^{-8}$	$1.528 \times 10^{-9}$	$7.193 \times 10^{-7}$	$3.808 \times 10^{-8}$
DPP-1	$1.833 \times 10^{-8}$	$5.774 \times 10^{-10}$	$3.023 \times 10^{-7}$	$2.108 \times 10^{-8}$
DPP-2	$1.900 \times 10^{-8}$	$1.732 \times 10^{-9}$	$8.887 \times 10^{-7}$	$4.384 \times 10^{-8}$
DPP-3	$1.767 \times 10^{-8}$	$4.163 \times 10^{-9}$	$8.087 \times 10^{-7}$	$1.207 \times 10^{-7}$
DPP-4	$1.833 \times 10^{-8}$	$1.528 \times 10^{-9}$	$9.453 \times 10^{-7}$	$3.329 \times 10^{-8}$
DPP-5	$1.933 \times 10^{-8}$	$1.528 \times 10^{-9}$	$9.650 \times 10^{-7}$	$1.242 \times 10^{-7}$
DPP-6	$2.067 \times 10^{-8}$	$1.155 \times 10^{-9}$	$1.007 \times 10^{-6}$	$3.894 \times 10^{-8}$
DPP-7	$1.767 \times 10^{-8}$	$5.774 \times 10^{-10}$	$1.070 \times 10^{-6}$	$1.416 \times 10^{-7}$
DPP-8	$1.900 \times 10^{-8}$	$1.000 \times 10^{-9}$	$1.034 \times 10^{-6}$	$1.331 \times 10^{-7}$
DPP-9	$2.200 \times 10^{-8}$	$2.000 \times 10^{-9}$	$1.091 \times 10^{-6}$	$3.747 \times 10^{-8}$
DPP-10	$2.667 \times 10^{-8}$	$5.774 \times 10^{-10}$	$1.146 \times 10^{-6}$	$6.295 \times 10^{-8}$

To compare with the vacuum simulations,  $R_g$  during the 10 ns production runs is analyzed. Table 3.7 lists the minimum, maximum, and average  $R_g$  of the average behavior of each glass model produced, both single- and multi-component. Immediately apparent is the small standard deviation in this average  $R_g$ , indicating that the structures in these glasses at 300 K do not experience large-scale unwinding. What is of note is that the values for  $R_g$  for all species are larger by 0.2 to 0.3 nm than the isolated self-solvated chains in the vacuum simulations, indicating interactions among components of the same chain allowing for relaxation of the collapsed structures seen in vacuum. The values of  $R_g$  also indicate that there are not rod-like conformations in any of the polymers, which would show a drastic increase in  $R_g$  compared to the rest of the data. This is like due to the polymers quickly self-solvating in the bulk simulation after the positional restraints were removed during equilibration. Instead, most structures seen are globular, stacked-rod, or coiled structures. The same holds for DPP-4T, the  $R_g$  values for which are listed in Table 3.8 for the 20-chain single component glass of DPP-4T and the singular DPP-4T chain in excess DPP-m chains. The same conclusions can be made as with the DPP-m moieties: a lack of

rod-like structures in favor of globular, stacked rod, and coiled configurations. However, it is significant to note that the standard deviation for the single-component DPP-4T (0.0007) is much lower than the single-component DPP-m species and for the multi-component species the singular DPP-4T chains experiences higher deviation in behavior than the DPP-m species. This is partly due to the number of samples used when calculating these averages and standard deviations, but also can be attributed to the higher rigidity and increased likelihood of more planar conformations along the backbone of DPP-4T. Figure 3.8 shows snapshots of the single-component systems to illustrate the type of structures seen.

Table 3.7: Radius of gyration ( $R_g$ ; nm) for DPP-m in different glass models.

polymer	single-component $R_g$ (nm)				multi-component $R_g$ (nm)			
	min.	max.	avg.	$\sigma$	min.	max.	avg.	$\sigma$
DPP-1	1.5717	1.5771	1.5741	0.0012	1.5076	1.5119	1.5097	0.0008
DPP-2	1.5412	1.5492	1.5468	0.0015	1.5381	1.5455	1.5411	0.0011
DPP-3	1.5908	1.5985	1.5960	0.0011	1.6424	1.6508	1.6449	0.0015
DPP-4	1.5841	1.5907	1.5884	0.0011	1.5664	1.5734	1.5694	0.0014
DPP-5	1.5775	1.5860	1.5828	0.0012	1.5914	1.5986	1.5937	0.0014
DPP-6	1.6340	1.6421	1.6399	0.0013	1.6148	1.6223	1.6171	0.0013
DPP-7	1.5596	1.5668	1.5640	0.0013	1.6067	1.6149	1.6091	0.0013
DPP-8	1.6129	1.6209	1.6184	0.0013	1.5951	1.6024	1.5979	0.0014
DPP-9	1.5944	1.6030	1.6005	0.0012	1.6041	1.6146	1.6079	0.0021
DPP-10	1.5848	1.5902	1.5873	0.0009	1.6276	1.6385	1.6316	0.0019

Table 3.8: Radius of gyration ( $R_g$ ; nm) for DPP-4T in different glass models.

polymer	$R_g$ (nm)			
	min.	max.	avg.	$\sigma$
<i>single-component</i>				
DPP-4T	1.9605	1.9640	1.9638	0.0007
<i>multi-component</i>				
DPP-1:DPP-4T	2.1332	2.1462	2.1404	0.0025
DPP-2:DPP-4T	2.1420	2.1659	2.1512	0.0037
DPP-3:DPP-4T	1.8636	1.8822	1.8742	0.0040
DPP-4:DPP-4T	2.0860	2.1024	2.0943	0.0029
DPP-5:DPP-4T	1.8470	1.8668	1.8572	0.0033
DPP-6:DPP-4T	2.0836	2.1054	2.0956	0.0033
DPP-7:DPP-4T	2.3596	2.3860	2.3710	0.0050
DPP-8:DPP-4T	1.9063	1.9274	1.9166	0.0045
DPP-9:DPP-4T	2.2395	2.2575	2.2479	0.0039
DPP-10:DPP-4T	1.5848	1.5902	1.5873	0.0009

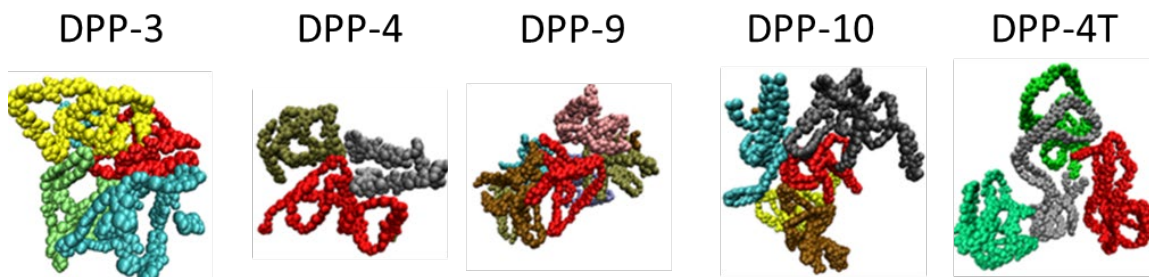


Figure 3.8: Simulation snapshots for selected polymers. Individual chains are represented with different colors. Some whole chains, all side-chain carbons, and all hydrogens removed from structures for clarity.

Continuing in the direct comparison of the gas and condensed-phase systems, the dihedral angle distributions for the same angle are extracted from the glass models. As mentioned previously, the thiophene-thiophene dihedral angle in DPP-4T is not expected to fluctuate much due to the  $\pi$ -conjugation. Figure 3.9 shows the dihedral angle

distributions of DPP-4T in the vacuum, single-, and multi-component systems. Compared to the vacuum system of a single self-solvated chain, the glass models show a much wider spread in the behavior of this dihedral angle. In the single-component DPP-4T system, the spread of values is shown to be much larger than in the gas-phase simulations, as can be seen by the wide range shown at  $180^\circ$ . Additionally, the peak at  $33^\circ$  shifts up to meet the same intensity as the peak at  $210^\circ$ . In the multi-component systems, DPP-4T is present as one chain surrounded by DPP-m chains. In these systems, the peak is also shifted down when compared to the vacuum simulation, but only by 0.0015. Overall, even though the peaks shift in height, they do not shift in angle value, so the  $180^\circ$  *trans*-conformation is still favored for this angle. It should be noted that in the glass models, there are chains for which the occurrence of the *trans*-conformation of this angle is reduced to 0.005, but for some chains in the same exact glass the peak is maxed at 0.020. Overall, this suggests consistent behavior among the monomer units in individual chains across different systems, as seen in the simulation snapshots in Figure 3.10. The structure of the DPP-4T chains (rose-colored) is fairly consistent no matter the chain that is surrounding it. This behavior may change as the population of DPP-4T:DPP-m increases, or the chain length of either species is changed, but in these systems the globular, stacked-rod, and coiled conformations appear to be preferred.

The DPP-m species also experience a shift in average behavior when comparing the vacuum and condensed-phase simulations. The inter-thiophene ring dihedral distributions are shown in Figure 3.11 for the vacuum and condensed-phase simulations. As with all other trends, DPP-1 exhibits deviation from the other DPP-m moieties by showing very little variation between the vacuum and condensed-phase angle distributions, still showing preference to the  $94^\circ$  and  $264^\circ$  conformations and lacking the  $180^\circ$  *trans*-oid conformation as the global maximum. The other DPP-m distributions in the condensed phases show similar structure to the vacuum simulations, but the intensity of peaks are reduced, smoothing the overall structure of the data. Additionally, the minimum occurrence (lowest value in the distribution) is raised as the length of the CBS unit increases, indicating that previously unfavorable conformations now occur more often. This effect is amplified in the DPP-10 systems to the extent that the distribution become pseudo-linear, indicating that all conformations are occurring near-equally. This of course comes from the flexibility of the CBS unit that connects the rings for which these distributions are defined. This lack of structure in the data can be seen among DPP-2 to DPP-9, where smaller length CBS have condensed-phase distributions structure similar to the vacuum simulations that is smoothed as the length increases. Thus as the length of the CBS increases more flexibility is granted to the chain.

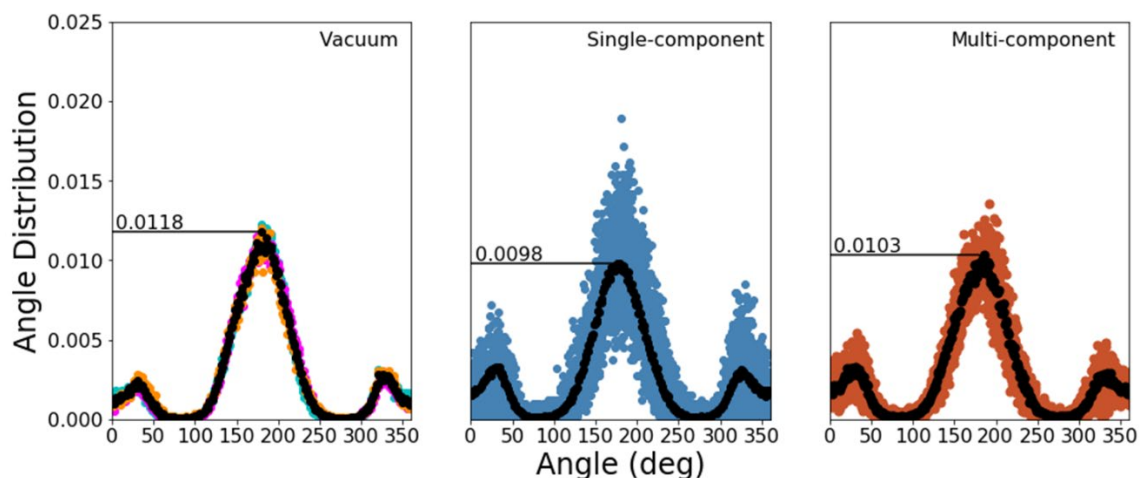


Figure 3.9: Dihedral angle distributions for the inter-thiophene angle in DPP-4T. LEFT: Vacuum simulations. MIDDLE: Single-component DPP-4T. RIGHT: Multi-component DPP-4T in DPP-m. In all three plots, the black points represent average behavior, colored points represent all behavior sampled.

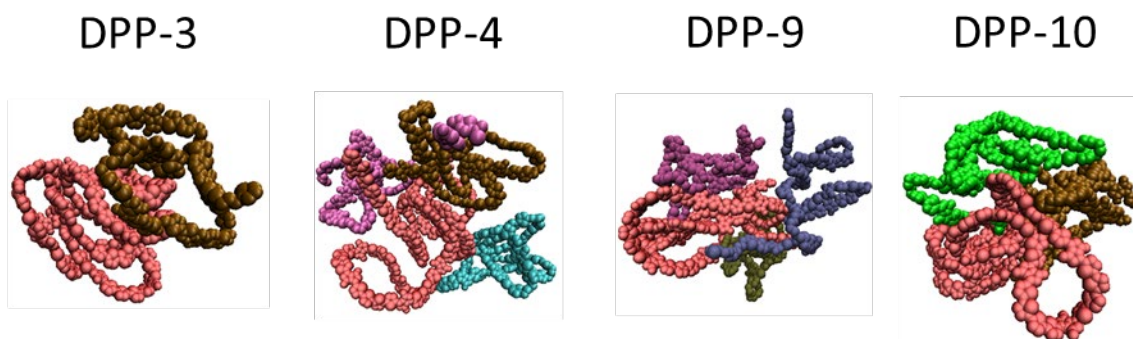


Figure 3.10: Simulation snapshots of the multi-component systems of DPP-4T in DPP-3, DPP-4, DPP-9, and DPP-10. The singular DPP-4T chain is rose-colored in all images, other DPP-m chains are given unique colors to distinguish individual chains. In all images, side chains and all hydrogens have been omitted for clarity.

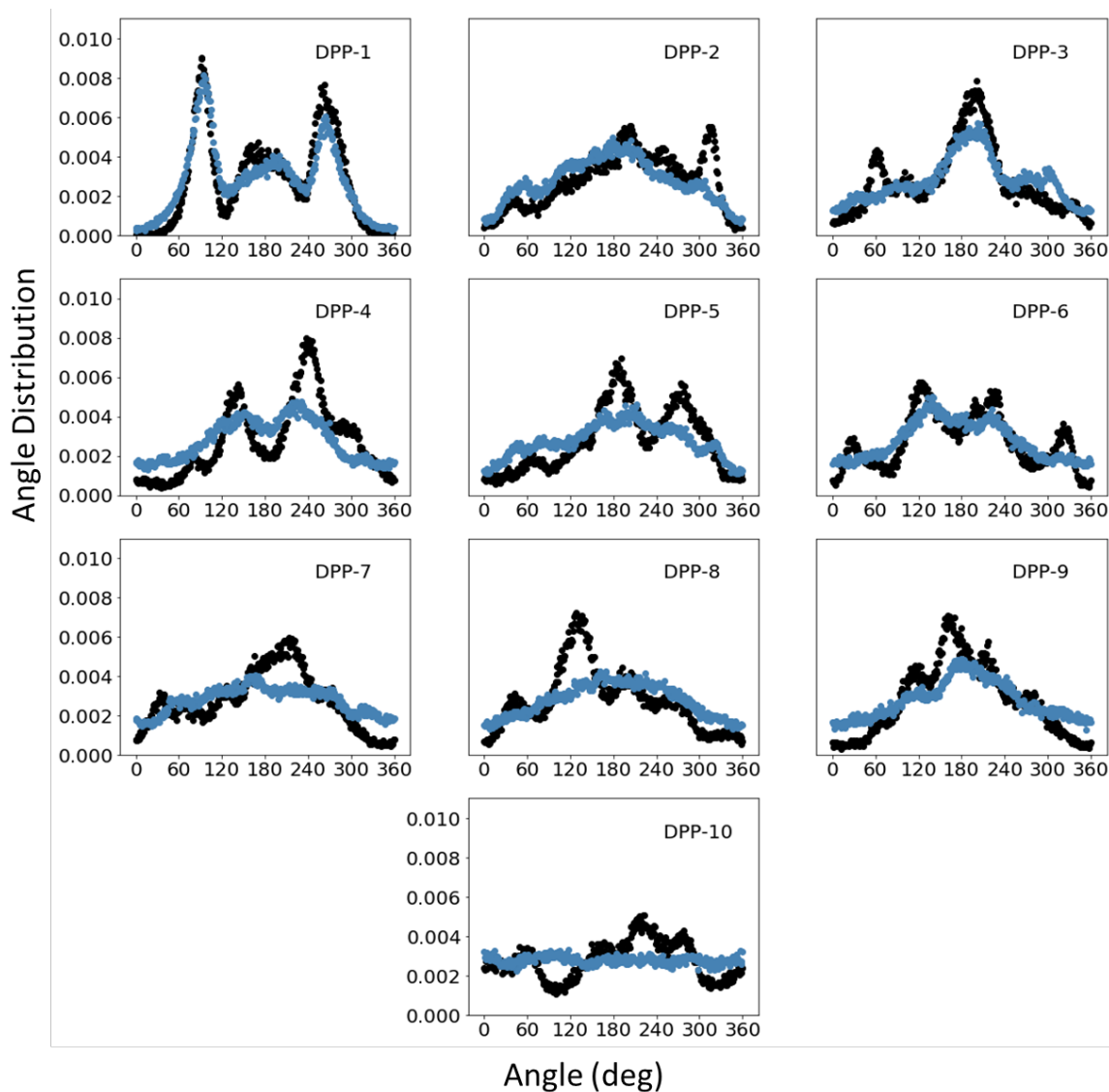


Figure 3.11: Vacuum (black) versus condensed-phase (blue, average of single- and multi-component systems) dihedral angle distributions. Histogram is binned at every whole-number angle from 0° to 360°. 180° represents a trans-oid configuration.

### 3.4 Conclusions

The development of new polymer-based OSC is reliant on an understanding of how chain synthesis, dynamics, and processing all impact the intra- and inter-chain interactions that further dictate material morphology. This work utilizes MD simulations to observe the structure of polymer chains in vacuum and various condensed phase environments and analyzing the effects of increasing flexibility by adding non-conjugated segments in the monomer structure. These simulations show that there is influence on the  $R_g$ , inter-ring torsion angles, self-diffusion, and density based on the length and the parity of the CBS



unit. Future work on these systems is to investigate larger condensed-phases for their behavior compared to others, as well as the inclusion of solution-phase simulations to discern the impact that different solvents will have with different lengths of CBS insertions. Additionally, stress-strain relationships can be investigated through simulations of systems with an applied force. An aspect not discussed in this work is the effect of the alkyl side chains on the structure. In these DPP-based polymers, the side chains are long and bulky, and in simulations have shown a common behavior of either interdigitating with other side chains, flattening and conforming to the shape of the backbone, or filling space and maximizing hydrophobic interactions, possibly leading to the preference for globular and coiled polymer structures. As with all OSC, the connection between the structures of polymer blends to charge-carrier transport should also be investigated so that the relevant components can be included in the design of better materials.

## CHAPTER 4. BEHAVIOR OF POLYMER AND SMALL MOLECULE BLENDS

### 4.1 Introduction

As discussed in Section 1.3, a common material setup for a BHJ device is to combine a  $\pi$ -conjugated polymer with a small-molecule acceptor (SMA), which here means any non-polymer species, as these ‘small molecules’ can themselves be larger than the monomer structure used in the material. An early development in OPV was the use of fullerene-based acceptors (FBA) in the OSC blends, favored for their high packing order and resulting excellent electron mobility. However, aggregates of FBA can quickly create an internal domain that is too large for efficient charge transport, and in the polymer-blended regions often lead to high disorder since packing with a polymer is unfavorable. In addition, their light harvesting properties are severely limited to the blue region of the spectrum. Due to these reasons, developing non-fullerene acceptors (NFA) has become popular in the field.<sup>32,33</sup> While the FBA had good mobilities for organic species at the beginning of their development, the advent of these NFA species quickly set a new standard, especially given their relatively easier synthesis over FBA species.

The internal structure of an OSC heavily influences the performance of the device it is a part of. With polymers as one of the components, finding ways to describe this internal structure becomes a difficult problem. The work in this chapter investigates the morphologies of various polymer-SMA systems for trends in the chemical structure and molecular behavior, and if there might be a relationship between the two. The species investigated are shown in Figure 4.1 labeled with their common abbreviated name. Many of these species have been used in various combinations to produce OPV devices with good PCE.

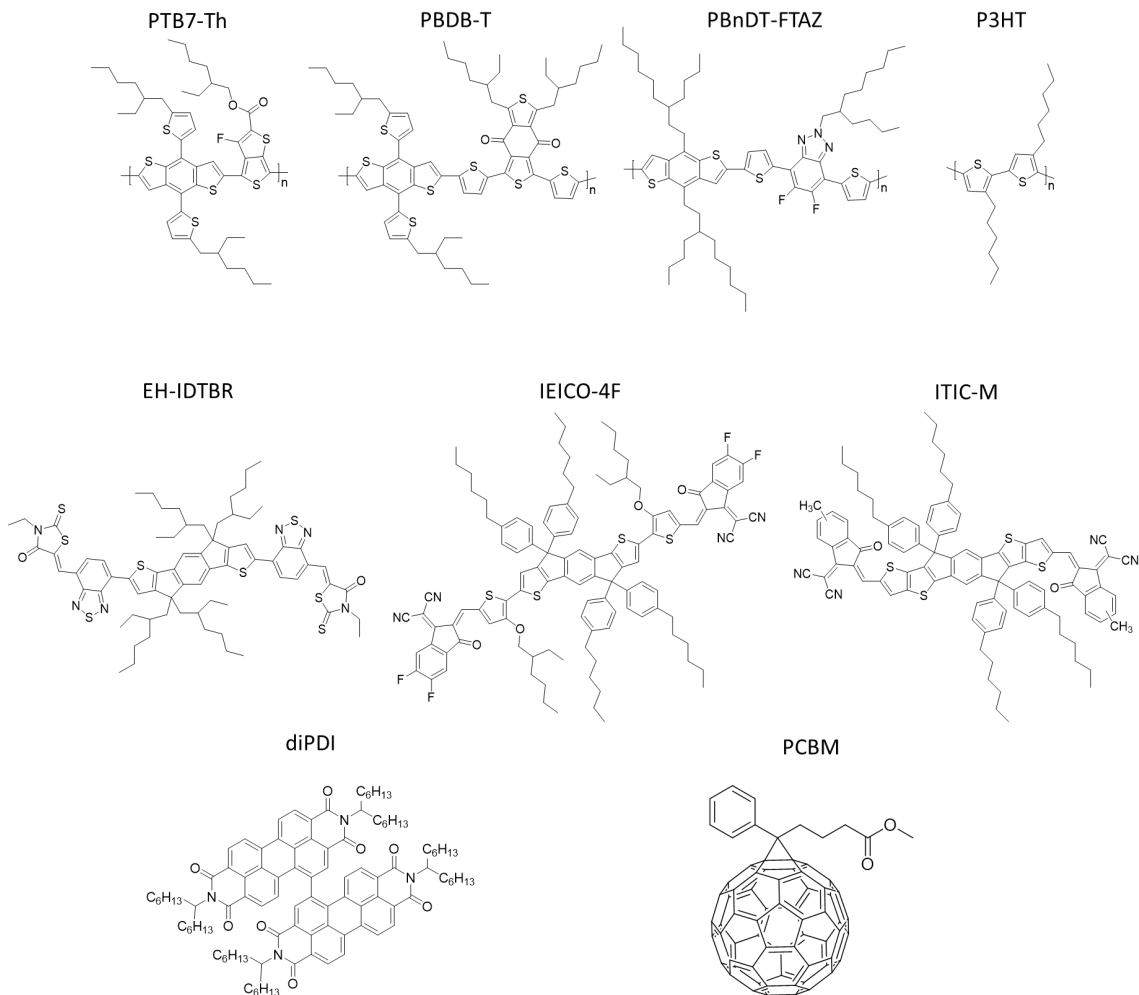


Figure 4.1: Structures of the BHJ component species investigated in this work. Four polymers, PTB7-Th, PBDB-T, PBnDT-FTAZ, and P3HT are blended with various acceptors: EH-IDTBR, IEICO-4F, ITIC-M, diPDI, and PCBM.

## 4.2 Methods

Details regarding the force field and software used follow the discussions in chapter 2. The number of atoms and the weights of each chain or SMA are listed in Table 4.1. To examine a wide variety of structures, 14 different blends were simulated at three different amounts of each component: one polymer chain in 100 SMA, one SMA in ten polymer chains, and then a 1:1 mass ratio blend. The mass ratios and percent SMA are listed in Table 4.2, excluding the 1:1 blend which is all  $50\% \pm 0.05\%$ . Additionally, single-component systems of the individual polymers and SMA were observed for base comparisons of the individual species' properties.

Table 4.1: Atom counts and weights for the DPP-4T and DPP-m polymer chains used in this work.

<b>Polymer</b>	<b>Atom Count</b>	<b>Weight (Da)</b>
PTB7-TH (32)	3682	28462
PBDB-T (19)	2966	22496
PBnDT-FTAZ (19)	2852	19291
P3HT (99)	2477	16464
<b>SMA</b>		
EH-IDTBR	176	1326
IEICO-4F	244	1810
ITIC-M	186	1456
diPDI	210	1396
PCBM	88	911

Table 4.2: Mass percent SMA for the systems not at equal mass ratio (1:1 blends)

Polymer	SMA	Percent SMA	
		10 chains: 1 SMA	100 SMA : 1 chain
PTB7-Th	EH-IDTBR	0.464	0.823
	IEICO-4F	0.632	0.864
	ITIC-M	0.509	0.836
	diPDI	0.488	0.831
PBDB-T	EH-IDTBR	0.586	0.855
	IEICO-4F	0.798	0.889
	ITIC-M	0.643	0.866
	diPDI	0.617	0.861
PBnDT-FTAZ	EH-IDTBR	0.683	0.873
	IEICO-4F	0.930	0.904
	ITIC-M	0.749	0.883
	diPDI	0.718	0.879
P3HT	EH-IDTBR	0.799	0.890
	PCBM	0.550	0.847

All simulations follow the same initialization, equilibration, and production simulations. For the single-component systems, 100 SMA or 10 polymer chains were randomly inserted into a simulation space such that was then readjusted to make sure no atom was within 2 nm of the box edge, resulting in 9 different systems. The 1:1 blend systems were initialized in a similar way, starting with the insertion of 10 polymer chains and then enough of the SMA species to reach the appropriate mass ratio, again ensuring no atom was within 2 nm of the box edge. The 1:1 blends add another 14 systems. Both other multi-component systems (1 chain/SMA in many SMA/chains), we initialized by centering the species that will be included only once in the center of the box, and then randomly inserting the bulk around it, creating another 28 systems, which brings the total number of systems simulated to 51. All systems were simulated in triplicate with unique starting configurations, yielding a total of 153 final trajectories.

After generating the initial coordinates, the 153 individual systems were all run through a similar equilibration scheme as that shown in section 3.2, the steps of which are listed in Table 4.3. The NPT compression steps all used a temperature coupling constant of 0.1 ps and a velocity rescaling thermostat and a pressure coupling constant of 2 ps with the Berendsen barostat. Equilibration and production NPT steps use the Parrinello-Rahman barostat. Positional restraints are enforced to prevent polymer self-solvation through step 14 as detailed in Table 4.3. The hydrogen bonds are again constrained with the LINCS algorithm. Following equilibration, a 10 ns NPT simulation is used to generate the trajectories that will be analyzed.

Table 4.3: Compression and decompression steps for all systems investigated.

step	conditions	duration (ns)
1	NVT 550 K	2
2	NVT 300 K	2
3	NPT 1000 bar, 300 K	2
4, 5	NVT 550 K, NVT 300 K	1,2
6	NPT 2500 bar, 300 K	2
7, 8	NVT 550 K, NVT 300 K	1,2
9	NPT 1000 bar, 300 K	2
10, 11	NVT 550 K, NVT 300 K	1,2
12	NPT 500 bar, 300 K	2
13	NVT 300 K	2
14, 15	NPT 1 bar, 300 K	2,10

### 4.3 Results and Discussion

Attention is first turned to the single-component systems to establish a baseline with which to compare the multi-component systems. The density, self-diffusion coefficients, and the radius of gyration for the various single-component systems are listed in Table 4.4, with the values representing the average of three unique simulations. Some initial conclusions can start to be formed, notably among the density and radius of gyration of the various species. First, it is important to note the inverse relationship between the computed condensed-polymer density and the corresponding  $R_g$ , which is expected. As the average distance from the center of mass for a chain increases in all directions, it takes up more space and thus decreases the average density. While this relationship is maintained for the SMA, the traditional definition of the radius of gyration does not apply to these species, but the mathematical definition is useful for describing shape. For the polymer chains, it should be noted that the values at room temperature versus the elevated temperature follow what is expected for changing the temperature, i.e. at a higher temperature the density decreases, the self-diffusion increases, and the  $R_g$  increases, indicating that chains are more extended. For the SMA species, the trends in the density and self-diffusion are maintained, yet the  $R_g$  does not always increase. It is apparent by the relatively small change in  $R_g$  for these species that thermal fluctuations are not going to drastically impact the molecular geometry, as would be expected for a  $\pi$ -conjugated species, especially the more planar variety (EH-IDTBR, IEICO-4F, and ITIC-M).

Table 4.4: Computed metrics for the single-component polymer and SMA systems

Polymer	Density (g/cm <sup>3</sup> )		Diffusion (cm <sup>2</sup> /sec) x 10 <sup>-5</sup>		R <sub>g</sub> (nm)	
	(298K)	(550K)	(298K)	(550K)	(298)	(550)
PTB7-TH (32)	1.222	1.047	0.0013	0.0351	3.239	3.411
PBDB-T (19)	1.213	1.038	0.0011	0.0413	2.843	2.929
PBnDT- FTAZ (19)	1.134	0.973	0.0009	0.0052	3.681	4.238
P3HT (99)	1.283	1.094	0.0014	0.0466	2.816	2.937
<b>SMA</b>						
EH-IDTBR	1.217	1.040	0.0013	0.1199	0.772	0.763
IEICO-4F	1.155	0.962	0.0032	0.1915	0.803	0.816
ITIC-M	1.209	0.994	0.0022	0.1590	0.736	0.742
diPDI	1.246	1.086	0.0019	0.1877	0.615	0.603
PCBM	1.384	1.136	0.0015	0.1362	0.449	0.447

A trend can also be found in the self-diffusion coefficients and the  $R_g$ . As seen with the polymer data in Table 4.4, the larger  $R_g$  values correspond with a less diffusive material. This is also expected as larger  $R_g$  stems from a more spread-out polymer chain conformation, which would take up more space and restrict the movement within the bulk. Moving to the SMA species, of note is the reduced diffusion for EH-IDTBR, which is the most planar species studied here. This value, coupled with the value obtained for PCBM seems to suggest that the more planar a molecule is, the less diffusive it is in single-component condensed-phase bulk. This conclusion also is more dependent on the overall  $\pi$ -conjugated core rigidity rather than the number of rings, as IEICO-4F, which has a 7-membered ladder system at its core, is more diffusive than EH-IDTBR and ITIC-M.

Moving now to the multi-component systems, each property in Table 4.4 is observed separately over all types of blends. Starting with the density, the 1:1 blends all have smaller densities than their pure counterparts. This is expected, as the introduction of a new chemical species into a pristine bulk will disrupt the order and increases the molecular volume, thus decreasing the density. When looking at the other two blends, initial conjecture may lead to assuming their density will be close to the density of the species that is in higher concentration. However, since these are mass ratios and the chains are fairly long, even the systems of 1 polymer chain in 100 SMA are less than 1% SMA by mass. For this reason, the density of all the systems is not that varied across all mass ratios. Since the blends are mostly polymer mass, it might be expected that the density patterns will follow that seen in the density of the polymers in pristine bulk. This trend does hold in that all the blends for P3HT have the highest densities, followed by PTB7-Th, PBDB-T, and then PBnDT-FTAZ. Within each of these, it appears that combing the polymers

with diPDI produces the densest blend, followed by EH-IDTBR, ITIC-M, and then IEICO-4F. For the P3HT blends, PCBM results in denser systems than EH-IDTBR.

Table 4.5: Calculated densities for the various polymer:SMA blends .

System:	Density (g/cm <sup>3</sup> )					
	T=298K			T=550K		
	1:1 blend	1 chain: 100 SMA	1 SMA: 10 chains	1:1 blend	1 chain: 100 SMA	1 SMA: 10 chains
<b>PTB7-Th</b>						
IEICO-4F	1.189	1.165	1.223	1.006	0.973	1.047
ITIC-M	1.198	1.182	1.223	1.023	1.006	1.047
diPDI	1.238	1.238	1.223	1.088	1.094	1.048
IDTBR	1.216	1.212	1.223	1.043	1.041	1.046
<b>PBDB-T</b>						
IEICO-4F	1.183	1.162	1.210	1.000	0.971	1.039
ITIC-M	1.192	1.179	1.210	1.019	1.003	1.042
diPDI	1.232	1.235	1.210	1.092	1.102	1.048
IDTBR	1.210	1.210	1.210	1.040	1.040	1.039
<b>FTAZ</b>						
IEICO-4F	1.148	1.140	1.164	0.941	0.916	0.962
ITIC-M	1.134	1.122	1.151	0.953	0.912	0.974
diPDI	1.189	1.189	1.203	0.986	0.9945	1.014
IDTBR	1.168	1.165	1.198	0.956	0.953	0.985
<b>P3HT</b>						
PCBM	1.144	1.141	1.168	0.945	0.927	1.021
IDTBR	1.125	1.119	1.134	0.920	0.907	0.924

In trying to relate the molecular structure to the trends in density, the polymers and SMA are best observed separately, and then together macroscopically. In the  $\pi$ -conjugated backbone it is note-worthy to keep track of at the number of rotatable bonds in the chains, as this is where the most motion in the backbone comes from. These rotatable bonds are restricted to fluctuating only 30°-40° at room temperature due to parameterization, but the consecutive rotation of these segments results in eventual bending of the chain. The chain lengths were selected so that the number of conjugated bonds is similar, around 390-400, but due to the structure of the monomer units this results in different amount of rotatable segments and forced planar segments. P3HT is just repeating thiophene rings, and as such has a rotatable bond every 4 bonds. With 99 repeat units, this results in 98 rotatable segments. In comparison, the monomer backbone structure of PTB7-Th is composed of two ringed segments, and the 32-unit chain results in 63 rotatable bonds. PBDB-T and PBnDT-FTAZ are chains of 19 units, and both have 4 rings in their monomer backbones, with a total of 75 rotatable segments. While the atomic volume never changes despite the conformation of the chain, a coiled or globular structure results in a void space and this can



influence the volume taken up by similar species. P3HT is the densest species in the single-component system as a result of being a very small monomer structure: just one ring with a hexyl chain. In comparison, PTB7-Th and PBDB-T use multi-ringed components and the common ethylhexyl side chain, while PBnDT-FTAZ uses the larger butyloctyl side chain. While the ethylhexyl chains extend to the same length as the side chain in P3HT, they additionally sterically interact with the rest of the polymer, thus resulting in a less compact structure.

The SMA species exhibit a wider variety of structures. Of these, ITIC-M, EH-IDTBR, and IEICO-4F have a similar mostly planar overall structure composed of a fused ring core with multiple other ringed components symmetrically out along the orientation of the backbone. They also all have side chains that can stick out away from the axis that the  $\pi$ -conjugated backbone lies on, whether the chains be the ethylhexyl used in the polymers or an extended phenyl-ethylhexyl. diPDI is composed of two perylenediimide (PDI) moieties attached by one rotatable bond that is much more locked in place, forcing the two units to remain close to perpendicular to each other. This yields in a slightly more voluminous structure in more directions, compared to the primarily one-dimensional extension of the other species. PCBM is the outlier here, as it is significantly spherical/ellipsoidal. It appears that based on the data in the single-component system, being more spherical results in a higher density, same with smaller side chains and a smaller core. It is interesting to note that generally, the trends seen in the density of the single-component systems are maintained in the multi-component systems, save for some of the higher temperature data points.

The self-diffusion for these systems is also of interest as a system that is less diffusive will be stable for longer, thus increasing the lifetime and overall effectiveness of the material as a device. The MSD-derived diffusion for the various polymer:SMA systems is listed in table 4.6. The trend in this data is less apparent than with the density data, but some structure-related conclusions can still be made. For the polymers, it appears that using components that extend out further with fused rings away from the backbone leads to a less diffusive material. Specifically, PBDB-T is the least diffusive, and uses both a benzodithiophene segment substituted on each side with thiophene rings and ethylhexyl groups and also another three-ringed segment that is a multi-substituted indacenedione. PTB7-Th uses the same thiophene-substituted benzodithiophene, and while it has only a two fused-ring segment, it includes both a fluorine and an oxygen that can easily repel against its own atoms and influence the neighboring molecules. PBnDT-FTAZ, while also containing fluorine and four separate ringed segments, has longer side chains with no thiophene spacers that can bend completely to align with the polymer backbone, thus reducing the space taken up by that small portion of the chain. Additionally, these chains could increase the hydrophobicity off the outer surface of the chain, which when in the presence of any other of the same chain or an SMA species with similar surface hydrophobicity, could lead to increased diffusion from van der Waals and dispersion forces. Lastly, P3HT is the smallest polymer simulated, and from a space-filling argument would lead to the most system movement, and thus the highest measured diffusion.

For the SMA species, the commentary on the influence of side chains applies again to these species. EH-IDTBR results in the most diffusive systems and is both the most planar species and uses the smallest side chains. In the case of P3HT:EH-IDTBR it does result in a less diffusive system than P3HT:PCBM, but as discussed previously the rounder nature of PCBM takes up more space and thus increases the overall motion. The next most diffusive SMA is diPDI, which given the space-filling argument makes sense especially compared to the structures of ITIC-M and IEICO-4F. While ITIC-M uses the same five-ringed indacenodithiophene core as EH-IDTBR, it and IEICO-4F both have phenylethylhexyl groups off their fused-ring core, with IEICO-4F also having two additional rings. In addition, both IEICO-4F and ITIC-M use a dicyano-substituted indanone segment on the outer portion of the backbone, additionally substituted with fluorine and a methyl group respectively. All of these additions reduce the motion of the system on the basis of sterics and electrostatics.

Table 4.6: Calculated MSD-derived diffusion for the various polymer:SMA blends .

System:	Diffusion (cm <sup>2</sup> /sec) x10 <sup>-5</sup>					
	T=298K			T=550K		
	1:1 blend	1 chain: 100 SMA	1 SMA: 10 chains	1:1 blend	1 chain: 100 SMA	1 SMA: 10 chains
<b>PTB7-Th</b>						
IEICO-4F	0.002	0.003	0.001	0.090	0.165	0.042
ITIC-M	0.001	0.002	0.001	0.035	0.139	0.044
diPDI	0.001	0.002	0.001	0.042	0.031	0.046
IDTBR	0.001	0.002	0.001	0.087	0.115	0.047
<b>PBDB-T</b>						
IEICO-4F	0.002	0.003	0.001	0.100	0.175	0.045
ITIC-M	0.001	0.002	0.001	0.101	0.151	0.043
diPDI	0.001	0.002	0.001	0.050	0.038	0.049
IDTBR	0.001	0.002	0.001	0.085	0.111	0.054
<b>FTAZ</b>						
IEICO-4F	0.002	0.002	0.001	0.039	0.043	0.039
ITIC-M	0.002	0.003	0.002	0.057	0.072	0.056
diPDI	0.002	0.003	0.002	0.057	0.070	0.056
IDTBR	0.003	0.004	0.002	0.060	0.054	0.060
<b>P3HT</b>						
PCBM	0.003	0.003	0.003	0.065	0.084	0.064
IDTBR	0.003	0.003	0.003	0.062	0.075	0.061

#### 4.4 Conclusions

Approaching the design of new materials with the motivation of optimizing the electronic properties will lead to quick advancement of individual chemicals, but not accommodating for the physical properties can have unintended effects on the material

efficiency. As seen here, the chemical structure has a direct influence on the density and diffusion of the materials, both pristine and multi-component. While connections between the side chains, donor and acceptor size, and the backbone rigidity are made to both density and diffusion, these conclusions do not immediately imply a relationship between the density and diffusion of any of these blended systems. There may be a relationship between these properties in the single-component bulks, but further work should be done with many more species before this can be confirmed. Continuing investigations in these polymer:SMA blends should include more of the chemical space, as while all these species had similarities, they were also drastically different. There are also many more polymers, fullerenes, and perylene-based molecules that are being used in devices, and understanding how they all influence material morphology is useful for designing future iterations of each type.

## CHAPTER 5. CONCLUSIONS AND FUTURE WORK

The investigations here begin with a question about whether a relationship between the chemical structure, the material morphology, and the resulting electronic properties can be found. By using MD simulations, the behavior of various  $\pi$ -conjugated polymers in different condensed-phase environments is analyzed and related to the differences in shape among the different molecules. Mathematically modeling the behavior of these polymer chains is a very large-scale problem, so being able to relate some of the system properties such as density and diffusion is an easier approach. The work done in these investigations shows multiple first steps toward developing relationships between the chemical structure and the material morphology. In the development of future materials, understanding how they will behave is crucial to selectively designing better semiconductors.

Polymer-polymer environments and interactions are observed through the simulation of various DPP-based polymers. Additionally, a breakage in the  $\pi$ -conjugated backbone of various lengths is inserted to observe the changes to chain flexibility and how this influences the folding of the polymer chain. Through analyzing the  $R_g$  over time as the polymer chains are allowed to transition from extended to a collapsed globule in a vacuum, it is found that increasing the length of the CBS unit increases the time it takes to collapse to a completely globular shape. Additionally, a pattern in odd-versus-even lengths is found in that the even-numbered CBS units result in a longer collapse time and a slower collapse rate than their odd-numbered counterparts. Turning to the condensed-phase systems, analysis of the single-component bulks shows that increasing the length of the CBS units increases the density, even if by a small amount. This leads to the conclusion that despite the addition of up to 30 new carbon and hydrogen atoms for DPP-10 (140 Da per added methylene unit), the resulting change in the volume overcomes the increase in mass. This specific change to the density further indicates that making the chains more flexible through alkyl insertions results in many more conformations available to the chains. Along with the density, the glass transition temperature is predicted through analysis of the density versus increasing temperature, as well as the diffusion. Both of these metrics show another odd-even trend, even if less-obvious. As expected, the smallest  $R_g$  available increases compared to that which is available to a self-solvated chain in vacuum. Analyzing the dihedral angle distribution between the thiophene rings that cap the CBS segment shows another odd-even pattern and a trend corresponding to increasing length. Moving to multi-component systems (one chain DPP-4T in bulk DPP-m), these trends are reinforced, even if less apparent.

The work in Chapter 3 is certainly a first step towards understanding the effect of the CBS insertions on the chain folding and the overall bulk morphology. This understanding can be further developed by finding new metrics to describe the specific bending of the chain, and an ideal product of these investigations would be a series of measures that can describe how any chain is folded without having to view a representation of the simulation trajectory. This way, analyzing other polymer species with any length of type of CBS

insertion can be performed more efficiently. Additionally, DPP-m has been synthesized up to 100 units, so analyzing longer lengths may yield more patterns on the microscale, since it has been shown that most length trends plateau after 11 units inserted. Finally, the analytical methods used to describe these polymers may be useful in describing the folding and behavior of other polymers, replacing the CBS units with ringed backbone components of similar lengths. Development of this technique would lead to more efficient analysis, thus more polymers can be observed, through which more design paradigms can be established.

The development of more efficient materials does not proceed on one single path. Often many different chemicals are investigated at the same time, resulting in competing materials and devices. Thus it is necessary to compare these varying species for connections between the chemical structure and the device performance. The work in Chapter 4 addresses this for four polymers and five SMA species. Through the analysis of density, system diffusion, and  $R_g$ , the components used to make these species are analyzed and shown to result in some trends. Specifically, the planarity vs sphericity, steric effects, and the size and type of solubilizing chains all have effects on the physical properties of the material. While these species are all significantly different in some way, there are many similarities. Future work into these polymer:SMA blends would be to traverse the chemical space between all of these species to look for trends related to the presence or lack of for a specific component. Similarly, all of the polymers contain thiophene rings somewhere in the monomer structure. Determining the effect of the amount of thiophene rings, as well as their locations in the structure, has on the chain behavior would be useful for future materials design, especially since thiophene is so common in so many OSC. Overall, more investigation into the various components needs to be done to be able to exactly confirm that their inclusion has a certain effect.

## REFERENCES

- (1) Fincher, C. R.; Ozaki, M.; Tanaka, M.; Peebles, D.; Lauchlan, L.; Heeger, A. J.; MacDiarmid, A. G. Electronic Structure of Polyacetylene: Optical and Infrared Studies of Undoped Semiconducting  $(\text{CH})_x$  and Heavily Doped Metallic  $(\text{CH})_x$ . *Phys. Rev. B* **1979**, *20* (4), 1589–1602. <https://doi.org/10.1103/PhysRevB.20.1589>.
- (2) Heimel, G.; Salzmann, I.; Duhm, S.; Koch, N. Design of Organic Semiconductors from Molecular Electrostatics. *Chem. Mater.* **2011**, *23* (3), 359–377. <https://doi.org/10.1021/cm1021257>.
- (3) Scheffler, M.; Dressel, M.; Jourdan, M.; Adrian, H. Extremely Slow Drude Relaxation of Correlated Electrons. *Nature* **2005**, *438* (7071), 1135–1137. <https://doi.org/10.1038/nature04232>.
- (4) Hasegawa, T.; Takeya, J. Organic Field-Effect Transistors Using Single Crystals. *Science and Technology of Advanced Materials* **2009**, *10* (2), 024314. <https://doi.org/10.1088/1468-6996/10/2/024314>.
- (5) Yamashita, Y. Organic Semiconductors for Organic Field-Effect Transistors. *Science and Technology of Advanced Materials* **2009**, *10* (2), 024313. <https://doi.org/10.1088/1468-6996/10/2/024313>.
- (6) Zhang, X.; Dong, H.; Hu, W. Organic Semiconductor Single Crystals for Electronics and Photonics. *Advanced Materials* **2018**, *30* (44), 1801048. <https://doi.org/10.1002/adma.201801048>.
- (7) Marcus, R. A.; Sutin, N. Electron Transfers in Chemistry and Biology. *Biochimica et Biophysica Acta (BBA) - Reviews on Bioenergetics* **1985**, *811* (3), 265–322. [https://doi.org/10.1016/0304-4173\(85\)90014-X](https://doi.org/10.1016/0304-4173(85)90014-X)
- (8) Mayer, A. C.; Scully, S. R.; Hardin, B. E.; Rowell, M. W.; McGehee, M. D. Polymer-Based Solar Cells. *Materials Today* **2007**, *10* (11), 28–33. [https://doi.org/10.1016/S1369-7021\(07\)70276-6](https://doi.org/10.1016/S1369-7021(07)70276-6).
- (9) Ryno, S. M.; Risko, C. Deconstructing the Behavior of Donor–Acceptor Copolymers in Solution & the Melt: The Case of PTB7. *Phys. Chem. Chem. Phys.* **2019**, *21* (15), 7802–7813. <https://doi.org/10.1039/C9CP00777F>.
- (10) Robertson, M. J.; Qian, Y.; Robinson, M. C.; Tirado-Rives, J.; Jorgensen, W. L. Development and Testing of the OPLS-AA/M Force Field for RNA. *J. Chem. Theory Comput.* **2019**, *15* (4), 2734–2742. <https://doi.org/10.1021/acs.jctc.9b00054>.
- (11) Dickson, C. J.; Madej, B. D.; Skjevik, Å. A.; Betz, R. M.; Teigen, K.; Gould, I. R.; Walker, R. C. Lipid14: The Amber Lipid Force Field. *J. Chem. Theory Comput.* **2014**, *10* (2), 865–879. <https://doi.org/10.1021/ct4010307>.

- (12) Wildman, J.; Repiščák, P.; Paterson, M. J.; Galbraith, I. General Force-Field Parametrization Scheme for Molecular Dynamics Simulations of Conjugated Materials in Solution. *J. Chem. Theory Comput.* **2016**, *12* (8), 3813–3824. <https://doi.org/10.1021/acs.jctc.5b01195>.
- (13) Berendsen, H. J. C.; Postma, J. P. M.; van Gunsteren, W. F.; DiNola, A.; Haak, J. R. Molecular Dynamics with Coupling to an External Bath. *J. Chem. Phys.* **1984**, *81* (8), 3684–3690. <https://doi.org/10.1063/1.448118>.
- (14) Braun, E.; Moosavi, S. M.; Smit, B. Anomalous Effects of Velocity Rescaling Algorithms: The Flying Ice Cube Effect Revisited. *J. Chem. Theory Comput.* **2018**, *14* (10), 5262–5272. <https://doi.org/10.1021/acs.jctc.8b00446>.
- (15) Bussi, G.; Donadio, D.; Parrinello, M. Canonical Sampling through Velocity Rescaling. *J. Chem. Phys.* **2007**, *126* (1), 014101. <https://doi.org/10.1063/1.2408420>.
- (16) Parrinello, M.; Rahman, A. Crystal Structure and Pair Potentials: A Molecular-Dynamics Study. *Phys. Rev. Lett.* **1980**, *45* (14), 1196–1199. <https://doi.org/10.1103/PhysRevLett.45.1196>.
- (17) Di Pierro, M.; Elber, R.; Leimkuhler, B. A Stochastic Algorithm for the Isobaric–Isothermal Ensemble with Ewald Summations for All Long Range Forces. *J. Chem. Theory Comput.* **2015**, *11* (12), 5624–5637. <https://doi.org/10.1021/acs.jctc.5b00648>.
- (18) Hess, B.; Bekker, H.; Berendsen, H. J. C.; Fraaije, J. G. E. M. LINCS: A Linear Constraint Solver for Molecular Simulations. *Journal of Computational Chemistry* **1997**, *18* (12), 1463–1472. [https://doi.org/10.1002/\(SICI\)1096-987X\(199709\)18:12<1463::AID-JCC4>3.0.CO;2-H](https://doi.org/10.1002/(SICI)1096-987X(199709)18:12<1463::AID-JCC4>3.0.CO;2-H).
- (18) Hess, B.; Bekker, H.; Berendsen, H. J. C.; Fraaije, J. G. E. M. LINCS: A Linear Constraint Solver for Molecular Simulations. *Journal of Computational Chemistry* **1997**, *18* (12), 1463–1472. [https://doi.org/10.1002/\(SICI\)1096-987X\(199709\)18:12<1463::AID-JCC4>3.0.CO;2-H](https://doi.org/10.1002/(SICI)1096-987X(199709)18:12<1463::AID-JCC4>3.0.CO;2-H).
- (19) Spoel, D. V. D.; Lindahl, E.; Hess, B.; Groenhof, G.; Mark, A. E.; Berendsen, H. J. C. GROMACS: Fast, Flexible, and Free. *Journal of Computational Chemistry* **2005**, *26* (16), 1701–1718. <https://doi.org/10.1002/jcc.20291>.
- (20) Hess, B.; Kutzner, C.; van der Spoel, D.; Lindahl, E. GROMACS 4: Algorithms for Highly Efficient, Load-Balanced, and Scalable Molecular Simulation. *J. Chem. Theory Comput.* **2008**, *4* (3), 435–447. <https://doi.org/10.1021/ct700301q>.
- (21) Zhou R., Liang, Q., and Yang, J. A Complete OSV-MP2 Analytical Gradient Theory for Molecular Structure and Dynamics Simulations. **2019**

(22) Gaussian 16, Revision C.01, Frisch, M. J.; Trucks, G. W.; Schlegel, H. B.; Scuseria, G. E.; Robb, M. A.; Cheeseman, J. R.; Scalmani, G.; Barone, V.; Petersson, G. A.; Nakatsuji, H.; Li, X.; Caricato, M.; Marenich, A. V.; Bloino, J.; Janesko, B. G.; Gomperts, R.; Mennucci, B.; Hratchian, H. P.; Ortiz, J. V.; Izmaylov, A. F.; Sonnenberg, J. L.; Williams-Young, D.; Ding, F.; Lipparini, F.; Egidi, F.; Goings, J.; Peng, B.; Petrone, A.; Henderson, T.; Ranasinghe, D.; Zakrzewski, V. G.; Gao, J.; Rega, N.; Zheng, G.; Liang, W.; Hada, M.; Ehara, M.; Toyota, K.; Fukuda, R.; Hasegawa, J.; Ishida, M.; Nakajima, T.; Honda, Y.; Kitao, O.; Nakai, H.; Vreven, T.; Throssell, K.; Montgomery, J. A., Jr.; Peralta, J. E.; Ogliaro, F.; Bearpark, M. J.; Heyd, J. J.; Brothers, E. N.; Kudin, K. N.; Staroverov, V. N.; Keith, T. A.; Kobayashi, R.; Normand, J.; Raghavachari, K.; Rendell, A. P.; Burant, J. C.; Iyengar, S. S.; Tomasi, J.; Cossi, M.; Millam, J. M.; Klene, M.; Adamo, C.; Cammi, R.; Ochterski, J. W.; Martin, R. L.; Morokuma, K.; Farkas, O.; Foresman, J. B.; Fox, D. J. Gaussian, Inc., Wallingford CT, 2016.

(23) Rassolov, V. A.; Ratner, M. A.; Pople, J. A.; Redfern, P. C.; Curtiss, L. A. 6-31G\* Basis Set for Third-Row Atoms. *Journal of Computational Chemistry* **2001**, *22* (9), 976–984. <https://doi.org/10.1002/jcc.1058>.

(24) Mardirossian, N.; Head-Gordon, M.  $\omega$ B97X-V: A 10-Parameter, Range-Separated Hybrid, Generalized Gradient Approximation Density Functional with Nonlocal Correlation, Designed by a Survival-of-the-Fittest Strategy. *Phys. Chem. Chem. Phys.* **2014**, *16* (21), 9904–9924. <https://doi.org/10.1039/C3CP54374A>.

(25) Marenich, A. V.; Jerome, S. V.; Cramer, C. J.; Truhlar, D. G. Charge Model 5: An Extension of Hirshfeld Population Analysis for the Accurate Description of Molecular Interactions in Gaseous and Condensed Phases. *J. Chem. Theory Comput.* **2012**, *8* (2), 527–541. <https://doi.org/10.1021/ct200866d>.

(26) Facchetti, A.  $\pi$ -Conjugated Polymers for Organic Electronics and Photovoltaic Cell Applications. *Chem. Mater.* **2011**, *23* (3), 733–758. <https://doi.org/10.1021/cm102419z>.

(27) Zhao, Y.; Zhao, X.; Zang, Y.; Di, C.; Diao, Y.; Mei, J. Conjugation-Break Spacers in Semiconducting Polymers: Impact on Polymer Processability and Charge Transport Properties. *Macromolecules* **2015**, *48* (7), 2048–2053. <https://doi.org/10.1021/acs.macromol.5b00194>.

(28) Bijleveld, J. C.; Zoombelt, A. P.; Mathijssen, S. G. J.; Wienk, M. M.; Turbiez, M.; de Leeuw, D. M.; Janssen, R. A. J. Poly(Diketopyrrolopyrrole-terthiophene) for Ambipolar Logic and Photovoltaics. *J. Am. Chem. Soc.* **2009**, *131* (46), 16616–16617. <https://doi.org/10.1021/ja907506r>.

(29) Zhao, X.; Zhao, Y.; Ge, Q.; Butrouna, K.; Diao, Y.; Graham, K. R.; Mei, J. Complementary Semiconducting Polymer Blends: The Influence of Conjugation-Break Spacer Length in Matrix Polymers. *Macromolecules* **2016**, *49* (7), 2601–2608. <https://doi.org/10.1021/acs.macromol.6b00050>.



- (30) Newbloom, G. M.; Weigandt, K. M.; Pozzo, D. C. Structure and Property Development of Poly(3-Hexylthiophene) Organogels Probed with Combined Rheology, Conductivity and Small Angle Neutron Scattering. *Soft Matter* **2012**, *8* (34), 8854–8864. <https://doi.org/10.1039/C2SM26114F>.
- (31) Dyck, O.; Hu, S.; Das, S.; Keum, J.; Xiao, K.; Khomami, B.; Duscher, G. Quantitative Phase Fraction Detection in Organic Photovoltaic Materials through EELS Imaging. *Polymers* **2015**, *7* (11), 2446–2460. <https://doi.org/10.3390/polym7111523>.
- (32) Yan, C.; Barlow, S.; Wang, Z.; Yan, H.; Jen, A. K.-Y.; Marder, S. R.; Zhan, X. Non-Fullerene Acceptors for Organic Solar Cells. *Nature Reviews Materials* **2018**, *3* (3), 1–19. <https://doi.org/10.1038/natrevmats.2018.3>.
- (33) Duan, L.; Elumalai, N. K.; Zhang, Y.; Uddin, A. Progress in Non-Fullerene Acceptor Based Organic Solar Cells. *Solar Energy Materials and Solar Cells* **2019**, *193*, 22–65. <https://doi.org/10.1016/j.solmat.2018.12.033>.
- (34) Li, Y.; Gu, M.; Pan, Z.; Zhang, B.; Yang, X.; Gu, J.; Chen, Y. Indacenodithiophene: A Promising Building Block for High Performance Polymer Solar Cells. *J. Mater. Chem. A* **2017**, *5* (22), 10798–10814. <https://doi.org/10.1039/C7TA02562A>.

## VITA

Walker Mask

### **Education**

B.A. in Chemistry & Mathematics, Simpson College, Indianola, IA, May 2017

### **Professional Experience**

Research Assistant, University of Kentucky, Lexington, KY. Advisor: Dr. Chad Risko.  
May-Aug 2018, Jan-Dec 2019

Teaching Assistant, CHE 580 Computation and Data Science in Chemistry, University of Kentucky, Lexington, KY. Jan-May 2019

Teaching Assistant, General Chemistry, University of Kentucky, Lexington, KY. August 2017-Dec 2018

Teaching Assistant, Organic Chemistry, Simpson College, Indianola, IA. Jan-May 2016